Available online at www.sciencedirect.com

ScienceDirect

Geochimica et Cosmochimica Acta 230 (2018) 17–45

Geochimica et Cosmochimica Acta

www.elsevier.com/locate/gca

The impact of the Cretaceous–Paleogene (K–Pg) mass extinction event on the global sulfur cycle: Evidence from Seymour Island, Antarctica

James D. Witts [a,*], Robert J. Newton [a], Benjamin J.W. Mills [a], Paul B. Wignall [a], Simon H. Bottrell [a], Joanna L.O. Hall [a], Jane E. Francis [b], J. Alistair Crame [b]

[a] *Earth Surface Science Institute, School of Earth and Environment, University of Leeds, Woodhouse Lane, Leeds LS2 9JT, UK*
[b] *British Antarctic Survey, High Cross, Madingley Road, Cambridge CB3 0ET, UK*

Received 18 September 2017; accepted in revised form 23 February 2018; available online 10 March 2018

Abstract

The Cretaceous–Paleogene (K–Pg) mass extinction event 66 million years ago led to large changes to the global carbon cycle, primarily via a decrease in primary or export productivity of the oceans. However, the effects of this event and longer-term environmental changes during the Late Cretaceous on the global sulfur cycle are not well understood. We report new carbonate associated sulfate (CAS) sulfur isotope data derived from marine macrofossil shell material from a highly expanded high latitude Maastrichtian to Danian (69–65.5 Ma) succession located on Seymour Island, Antarctica. These data represent the highest resolution seawater sulfate record ever generated for this time interval, and are broadly in agreement with previous low-resolution estimates for the latest Cretaceous and Paleocene. A vigorous assessment of CAS preservation using sulfate oxygen, carbonate carbon and oxygen isotopes and trace element data, suggests factors affecting preservation of primary seawater CAS isotopes in ancient biogenic samples are complex, and not necessarily linked to the preservation of original carbonate mineralogy or chemistry. Primary data indicate a generally stable sulfur cycle in the early-mid Maastrichtian (69 Ma), with some fluctuations that could be related to increased pyrite burial during the 'mid-Maastrichtian Event'. This is followed by an enigmatic +4‰ increase in $\delta^{34}S_{CAS}$ during the late Maastrichtian (68–66 Ma), culminating in a peak in values in the immediate aftermath of the K–Pg extinction which may be related to temporary development of oceanic anoxia in the aftermath of the Chicxulub bolide impact. There is no evidence of the direct influence of Deccan volcanism on the seawater sulfate isotopic record during the late Maastrichtian, nor of a direct influence by the Chicxulub impact itself. During the early Paleocene (magnetochron C29R) a prominent negative excursion in seawater $\delta^{34}S$ of 3–4‰ suggests that a global decline in organic carbon burial related to collapse in export productivity, also impacted the sulfur cycle via a significant drop in pyrite burial. Box modelling suggests that to achieve an excursion of this magnitude, pyrite burial must be reduced by >15%, with a possible role for a short term increase in global weathering rates. Recovery of the sulfur cycle to pre-extinction values occurs at the same time (~320 kyrs) as initial carbon cycle recovery globally. These recoveries are also contemporaneous with an initial increase in local alpha diversity of marine macrofossil faunas, suggesting biosphere-geosphere links during recovery from the mass extinction. Modelling further indicates that concentrations of sulfate in the oceans must have been 2 mM, lower than previous estimates for the Late Cretaceous and Paleocene and an order of magnitude lower than today.

Keywords: Sulfur isotopes; $\delta^{34}S$; Cretaceous-Paleogene boundary; Mass extinction; Global sulfur cycle; Antarctica

* Corresponding author at: Division of Paleontology (Invertebrates), American Museum of Natural History, Central Park West & 79th Street, New York, NY 10024, USA.
E-mail address: jwitts@amnh.org (J.D. Witts).

https://doi.org/10.1016/j.gca.2018.02.037
0016-7037/

1. INTRODUCTION

The Cretaceous–Paleogene (K–Pg) mass extinction event of 66 Ma is not only the most recent of the Phanerozoic 'Big Five' mass extinctions (Bambach, 2006), but also the most well-known and best-studied. The leading hypothesis for the cause of this extinction remains a major bolide impact (Alvarez et al., 1980) and the consequential rapid and severe global environmental changes (Schulte et al., 2010). However, the K–Pg extinction event occurred during a time of longer-term environmental changes. These include climate (Wilf et al., 2003; Bowman et al., 2013; Thibault, 2016) and sea level fluctuations (Kominz et al., 2008; Haq, 2014), and large igneous province (LIP) volcanism from the Deccan Traps in India (Schoene et al., 2015; Renne et al., 2015). There remains significant debate as to the importance and relative contributions of each of these to the extinction event itself (e.g. Archibald et al., 2010; Courtillot and Fluteau, 2010; Keller et al., 2010; Schmidt et al., 2016), and even the possibility of cause-and-effect relationships between the impact event and voluminous Deccan volcanism (Richards et al., 2015; Renne et al., 2015).

Like other mass extinction events throughout Earth history, the K–Pg extinction led to changes to the global carbon cycle (Kump, 1991). A significant body of evidence suggests that the extinction was followed by a decrease in the primary and export productivity of the oceans. This is seen in the collapse of the vertical gradient in $\delta^{13}C$ between surface and deep-water dwelling foraminifera (Hsü and McKenzie, 1985; Zachos et al., 1989; D'Hondt, 2005; Birch et al., 2016), a proxy for the biological carbon pump; sinking of organic matter to deep water with associated remineralisation releasing ^{12}C to the surrounding water. Reduced carbonate accumulation rates, a decrease in values of bulk carbonate $\delta^{13}C$, and little or no offset in $\delta^{13}C$ between benthic and planktonic taxa characterise the initial aftermath of the K–Pg extinction in many deep ocean sites (Zachos et al., 1989; D'Hondt, 2005; Birch et al., 2016) and in shelf sections (Esmeray-Senlet et al., 2015) worldwide. Geochemical models suggest that a reduction of 30–40% in organic export or 10% reduction in organic carbon burial (Kump, 1991) is required to achieve the collapse in surface-deep $\delta^{13}C$ gradient (Birch et al., 2016).

In contrast to the carbon cycle, surprisingly little is known about how the global sulfur cycle may have responded to the events that surround the K–Pg mass extinction. Numerous factors drive the sulfur cycle and control the sulfur isotopic composition of seawater over geological timescales (Claypool, 1980; Berner and Canfield, 1989; Bottrell and Newton, 2006). Oxidative weathering of sulfide minerals and dissolution of evaporite deposits on land lead to the delivery of sulfate to the oceans via rivers (Claypool, 1980; Canfield, 2013), with volcanism and hydrothermal inputs also constituting a minor flux. Sulfur is removed from the ocean reservoir to the sediment either in an oxidised state (as carbonate associated sulfate (CAS), or evaporites, or in a reduced state (mainly FeS or FeS_2) following microbial sulfate reduction (MSR) in marine sediments (Canfield et al., 2010; Sim et al., 2011; Fike et al., 2015). Many of the Earth system changes that occurred during the K–Pg interval (e.g. climate change, sea level fluctuations, bolide impact and productivity collapse, LIP volcanism, anoxia) have the potential to affect aspects of the global sulfur cycle sufficiently to leave a stratigraphic record of isotopic change.

The ocean represents the largest reservoir of sulfur on the Earth's surface (Claypool, 1980). Sulfur as seawater sulfate has a long residence time (~10–20 Ma) and a relatively high concentration (29 mM) in the modern ocean (Bottrell and Newton, 2006), and therefore rapid perturbations to its sulfur isotope composition are unlikely. However, a variety of studies have demonstrated that during periods of major environmental change such as mass extinction events, rapid changes are recorded by CAS or pyrite isotopes. (e.g. Newton et al., 2004; Jones and Fike, 2013; Gomes and Hurtgen, 2016; Schobben et al., 2015). The occurrences of such changes has been explained by lower concentration of sulfate in ancient oceans, leading to concomitant lower residence times, allowing the cycle to respond rapidly to perturbations. As a result, examination of sulfur cycle changes through Earth history have the potential to provide new interpretations for the cause and effect of environmental change during mass extinction events.

As a proxy for reconstructing seawater sulfate isotopic composition, numerous studies have looked at CAS incorporated into biogenic carbonates. Studies on modern biota indicate that CAS in biogenic samples faithfully records the isotopic composition of ambient seawater in a variety of marine settings (e.g. Kampschulte et al., 2001; Kampschulte and Strauss, 2004; Lyons et al., 2004). CAS is resistant to diagenesis (Lyons et al., 2004; Marenco et al., 2008a, 2008b; Gill et al., 2008; Fichtner et al., 2017), and reproduces the record from other proxies for long-term Phanerozoic sulfur cycle changes such as evaporite minerals and marine barite (Claypool et al., 1980; Paytan et al., 1998; Paytan et al., 2004; Kampschulte and Strauss, 2004). Thus, CAS has proven to be a robust proxy for sulfur cycle changes during intervals of rapid environmental change throughout the Phanerozoic; including the end-Ordovician (Jones and Fike, 2013), late Devonian (John et al., 2010), and Permo–Triassic (Newton et al., 2004; Song et al., 2014; Schobben et al., 2015) extinction events and various Oceanic Anoxic Events (OAEs) (Adams et al., 2010; Newton et al., 2011; Gill et al., 2011; Owens et al., 2013; Poulton et al., 2015; Gomes et al., 2016).

Only two studies, from condensed deep water marine sections in Japan (Kajiwara et al., 1992) and Spain (Kaiho et al., 1999), have produced stratigraphically-constrained sulfur isotope records across the K–Pg boundary from the latest Cretaceous (Maastrichtian stage, 72.1–66 Ma) and earliest Paleogene (Danian stage, 66–61.6 Ma). The observed changes to the sulfur cycle at the K–Pg boundary are interpreted to record the development of a short period of ocean anoxia following the mass extinction event. However, only one study (Kaiho et al., 1999) produces a record from bulk rock CAS as a proxy for sea-

water sulfate. Both studies also cover an extremely restricted stratigraphic interval centred on the K–Pg boundary itself, which does not overlap with all the events that have a potential impact on the K–Pg mass extinction such as the possible effects of Deccan volcanism. Longer-term changes to the sulfur cycle during the Late Cretaceous or early Paleogene are poorly known, and existing datasets are of low resolution.

Under some circumstances, the isotopic signal from CAS can be altered towards either positive or negative values. The use of biogenic calcite and aragonite for CAS studies as opposed to bulk sedimentary carbonate reduces the risk of contamination of the primary isotope signal from sedimentary sulfide and its weathering products (Staudt and Schoonen, 1995; Kampschulte and Strauss, 2004). Biogenic carbonates also contain a higher concentration of CAS when compared to bulk sedimentary limestones, buffering them from diagenetic alteration (Staudt and Schoonen, 1995) and making them potentially the best source for the generation of CAS records. Nevertheless, careful consideration must still be made of possible diagenetic alteration and contamination of samples, as well as ensuring the data are placed in a sedimentary and palaeoenvironmental context before interpretation (e.g. Fike et al., 2015).

This study aims to generate such records from biogenic CAS, using fossils from an expanded and fossiliferous high latitude Cretaceous–Paleogene section located in the James Ross Basin, Antarctica. The overall aim is to examine sulfur cycle changes before, during, and after the K–Pg mass extinction event over a ~4 million-year time span.

2. GEOLOGICAL SETTING

Samples were collected from the shallow marine López de Bertodano Formation, which crops out over 70 km^2 of southern Seymour Island and neighbouring Snow Hill Island (Crame et al., 2004; Olivero et al., 2008), in the James Ross Basin, Antarctic Peninsula (Fig. 1A–D). The López de Bertodano Formation forms the upper part of the 3000 m-thick Marambio Group (McArthur et al., 2000; Crame et al., 2004; Olivero, 2012), and records mudstone-dominated deposition in inner-mid shelf conditions (Macellari, 1988; Olivero, 2012; Bowman et al., 2012) in a large back-arc basin (the Larsen Basin) which opened directly into the Weddell Sea to the east (Hathway, 2000). During the Late Cretaceous–Paleocene the Antarctic Peninsula, located to the west of present-day Seymour Island, was an active and emergent volcanic arc (Elliot, 1988; Hathway, 2000). Palaeogeographic reconstructions indicate that during the Late Cretaceous the James Ross Basin was located close to its present day high latitude of 65°S (Lawver et al., 1992). The López de Bertodano Formation itself is an unconformably-bound unit between the underlying Snow Hill Island Formation and overlying Sobral Formation (Olivero et al., 2008; Crame et al., 2014), and comprises ~1100 m of unlithified silty clays and clayey silts, with occasional glauconite–rich horizons especially in the uppermost 300 m (Macellari, 1988). The studied section contains no field evidence for significant hiatuses.

It is important to note that despite evidence for high resolution fluctuations in redox, possibly related to the polar light cycle and unique high latitude 'greenhouse' environment (Schoepfer et al., 2017), there is no evidence for tectonic restriction of the basin which could lead to the generation of local rather than global isotopic signatures. The López de Bertodano Formation contains a fully marine fauna (e.g. Macellari, 1988; Crame et al., 2004; Witts et al., 2016) indicative of open marine conditions. In addition, global changes in temperature and other palaeoceanographic events can be recognised in the basin (e.g. Tobin et al., 2012; Bowman et al., 2013).

An age model based on macrofossil and dinoflagellate biostratigraphy, strontium isotope chemostratigraphy, and magnetostratigraphy (McArthur et al., 1998; Crame et al., 2004; Tobin et al., 2012; Bowman et al., 2013; Witts et al., 2016), as well as the presence of an iridium (Ir) anomaly at the K–Pg boundary (Elliot et al., 1994), dates this unit as Maastrichtian–Danian. The sediment accumulation rates were high (0.1–0.2 mm/yr; Elliot et al., 1994; Bowman et al., 2013), and it is one of the most expanded sequences of this age anywhere in the world. The López de Bertodano Formation has thus been the subject of extensive palaeontological and stratigraphic studies over the last 30 years (Feldmann and Woodburne, 1988 and authors therein; Crame et al., 2004; Olivero, 2012; Bowman et al., 2012), and contains the best shallow-marine record in the Southern Hemisphere of the K–Pg mass extinction event (Zinsmeister, 1998; Witts et al., 2016).

Fossil molluscs from the James Ross Basin are generally thought to show excellent preservation, and have proved suitable for isotope analyses used to reconstruct palaeoceanographic conditions (e.g. Pirrie and Marshall, 1990; Ditchfield et al., 1994; McArthur et al., 2000; Tobin et al., 2012). This level of preservation is consistent with the idea that the sediments of the Marambio Group have undergone burial to minimal depths of 1–2 km at low temperatures and pressures (Askin and Jacobsen, 1988; Svojtka et al., 2009).

3. MATERIALS AND METHODS

Macrofossil samples were collected from southern Seymour Island during the 2006 field season of the British Antarctic Survey, and a composite measured section (D5.251) comprising several sections (in stratigraphic order; D5.212, .215, .218, .219, .220, .222, .229) was made through the entire 1074 m thickness of the López de Bertodano Formation (Fig. 1D). Sedimentary section lines were measured perpendicular to strike in the field using a Jacobs staff and Abney level and tape measure. Macrofossil collections were made at varying scales within each sub-section, with sample bins ranging on average from 1 m to intervals 5–6 m thick. All fossil occurrences are illustrated at the mid-point of the stratigraphic bin from which they were collected.

Examples of 6 different genera of bivalve mollusc were utilised in this study (Fig. 1E) covering a stratigraphic range

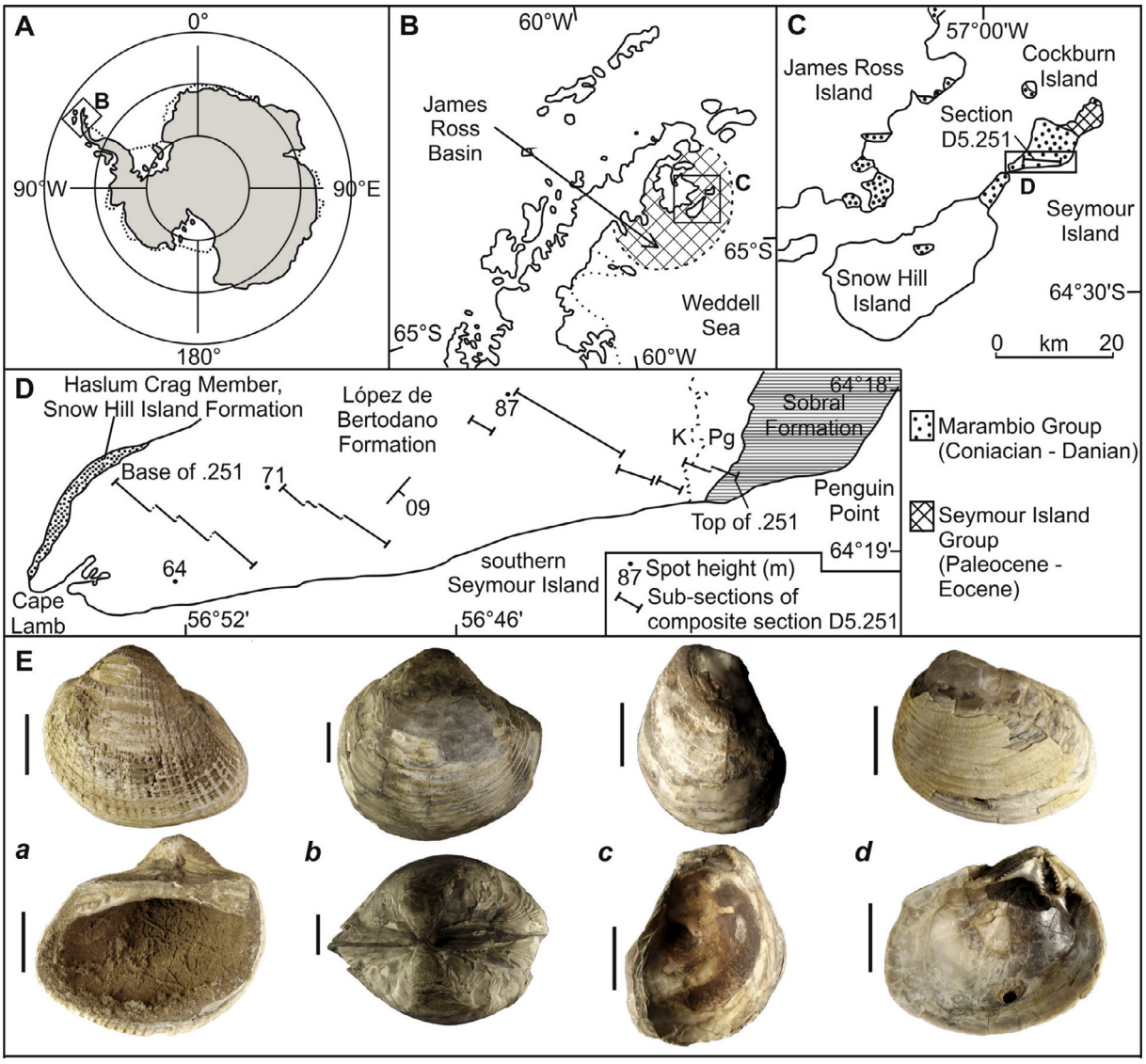

Fig. 1. Location map, geological setting, and images of fossil taxa used in this study. A–C, maps showing present-day geography of Antarctica (A) with the northern Antarctic Peninsula highlighted, location of the James Ross Basin (B), and outcrops of the Marambio and Seymour Island groups on islands in the James Ross Basin. D, measured section D5.251 across the southern portion of Seymour Island is a composite of various sub-sections (see Fig. 2 for more details). K, Cretaceous; Pg, Paleogene. Position of the K–Pg boundary in the upper portion of the López de Bertodano Formation is indicated by the dashed line. E, examples of fossil bivalve taxa from the López de Bertodano Formation sampled for CAS in this study. *a Cucullaea antarctica; b Lahillia larseni; c Pycnodonte* (*Pycnodonte*) *vesicularis; d Eselaevitrigonia regina.* All scale bars are 2 cm.

of 166–1074 m in the composite section (Fig. 2). Samples included representatives of the genera *Lahillia* (14 samples), *Cucullaea* (6 samples), *Eselaevitrigonia* (1 sample), *Oistotrigonia* (1 sample) (shallow infaunal suspension feeders), *Pycnodonte* (16 samples) (epifaunal suspension feeder) and *Leionucula* (1 sample) (deep infaunal deposit feeder) (Zinsmeister and Macellari, 1988). For this study, BAS samples numbers (D5. XXXX.2) were supplemented by a unique numbering system (X-1 or X-2) for ease of data visualisation (see Table 1 and Supplementary Information Tables S1 and S2 for details).

3.1. CAS ^{34}S extraction

CAS extraction was carried out using a modified version of a procedure developed at the University of Leeds (e.g. Newton et al., 2004; John et al., 2010; Newton et al., 2011). Fossil bivalve samples taken from composite BAS section D5.251 were screened visually to assess preservation, and shell material was picked from the specimens by hand or using a small chisel and tweezers. These were then washed in an ultrasonic bath for 20–30 min to remove any adhering sediment or matrix material. Between 2 and 4 g of

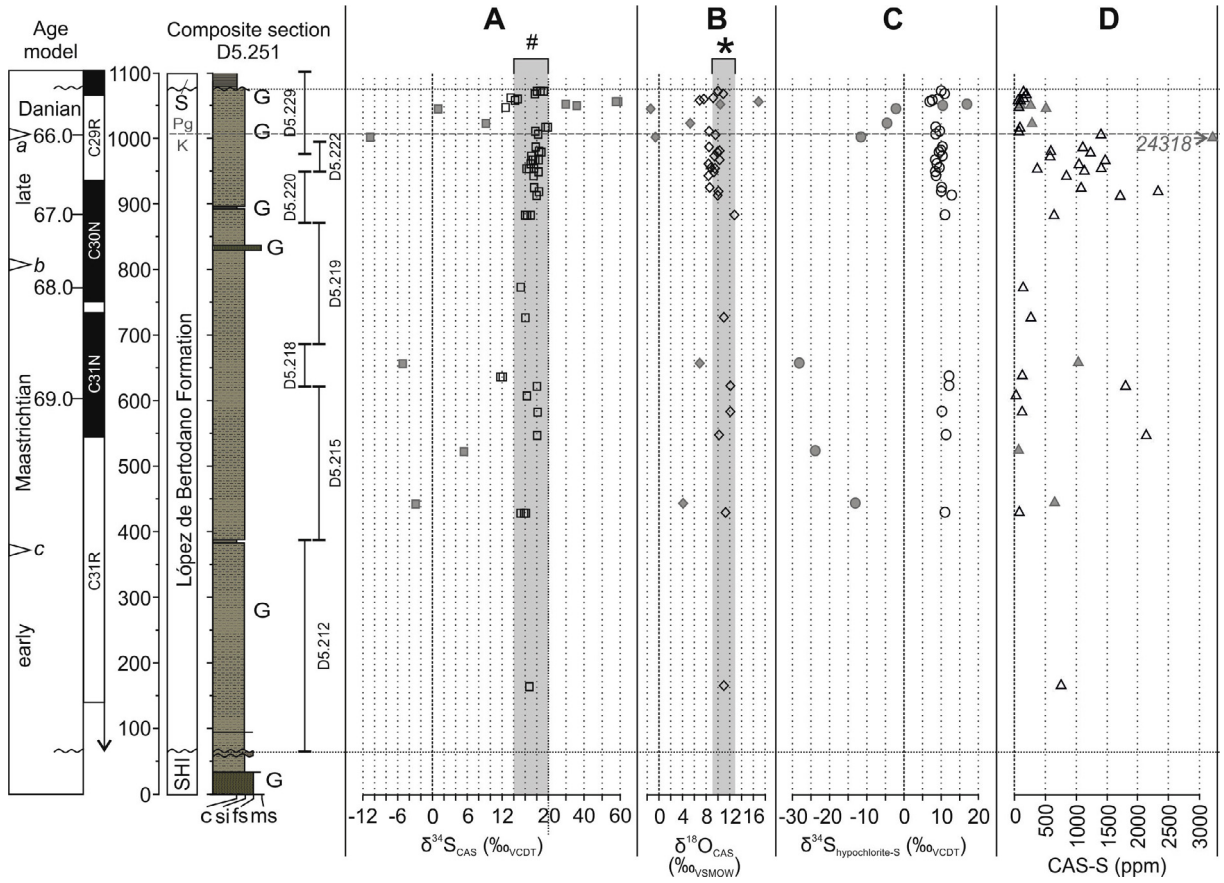

Fig. 2. A: $\delta^{34}S_{CAS}$ (open and filled squares), B: $\delta^{18}O_{CAS}$ (open and filled diamonds), C: $\delta^{34}S_{hypochlorite\text{-}S}$ (open and filled circles), D: CAS concentration data (open and filled triangles) from the López de Bertodano Formation. Filled symbols are datapoints considered unreliable through either contamination or alteration (see below). Vertical grey bars labelled # and * indicate the range of published $\delta^{34}S$ (from CAS and marine barite) and $\delta^{18}OS$ data respectively for the Maastrichtian–Paleocene intervals. Data from Claypool et al. (1980), Paytan et al. (1998; 2004), Kampschulte and Strauss (2004), and Turchyn and Schrag (2006). Number and arrow on D is single altered sample that plots outside the scale presented here. The sub-section overlap between D5.222 and D5.229 has been taken into account when plotting and interpreting the isotope data. Age model is derived from Bowman et al. (2013). Time scale is based on Sr isotope chemostratigraphy (italicized a–c) (McArthur et al., 1998) and magnetostratigraphy (Tobin et al., 2012), updated with ages from the Geological Time Scale 2012 (Gradstein et al., 2012) and using the K–Pg boundary datum. G, glauconite-rich intervals. S, Sobral Formation.

shell material was used for CAS analyses. A total of 58 shell samples were powdered by hand, and powdered samples were left in an excess of sodium hypochlorite (NaOCl) 5% for at least 24 h to remove sulfur contained in organic matter, sulfate, monosulfide minerals or pyrite (partially removed Wotte et al., 2012). Filtered NaOCl leachate was retained and its sulfate precipitated as $BaSO_4$ by adjusting the pH of the solution to 2.5–3.0 using hydrochloric acid (HCl), warming gently on a hotplate and adding excess 10% $BaCl_2$ solution at ~70 °C. Cellulose nitrate filter membranes were then weighed and used to filter the $BaSO_4$ precipitate. The weight of the $BaSO_4$ precipitate was measured to determine the NaOCl-S ($\delta^{34}S_{hypochlorite\text{-}S}$) yield.

The bleached and rinsed shell powders were reacted with 50% HCl in an anaerobic chamber to release the CAS from the calcite lattice and avoid oxidation of any surviving sulfide minerals (see Theiling and Coleman (2015) for a detailed discussion of the importance of completing this portion of the process under anaerobic conditions). 50% HCl was added until there was no more reaction. The solution was then filtered through a Whatman 40 filter paper to remove any residue. When the leachates were removed from the anaerobic chamber, they were immediately vacuum filtered through a 0.45 μm cellulose nitrate membrane. Great care was taken to minimise the amount of time during which the released CAS was present as dissolved sulfate in the acidic solution as isotopic exchange between sulfate-O and water-O is known to occur increasingly rapidly as pH decreases (Lloyd, 1967). The pH of the filtered solution was adjusted to >9.5 with concentrated ammonia solution and the samples left stirring overnight or longer in order to precipitate out any dissolved metals. Any precipitated metals and the leachate were separated using a Whatman 40 filter paper. Finally, $BaSO_4$ was precipitated from the HCl leachate by adjusting the pH to between 2.5 and 3 with HCl and ammonia solution, and adding 10% $BaCl_2$ solution in excess at ~70 °C. The weight of the $BaSO_4$ precipitate was measured to determine the

Table 1
Full list of samples and their stratigraphic context within composite stratigraphic section D5.251, sulfate sulfur ($\delta^{34}S_{CAS}$), sulfate oxygen ($\delta^{18}O_{CAS}$), bleached sulfate sulfur ($\delta^{34}S_{hypochlorite\text{-}S}$) isotope results, and CAS concentration.

Sample #	BAS Sample #	Comp. strat. height (M)	ID	$\delta^{34}S_{CAS}$ (‰VCDT)	$\delta^{18}O_{CAS}$ (‰VSMOW)	$\delta^{34}S_{hypochlorite\text{-}S}$ (‰VCDT)	[CAS] ppm
39-1	D5.1379.2	1074	*Lahillia*	18.7	10.0	8.0	148
38-1	D5.1375.2	1070	*Lahillia*	17.6	10.9	−10.5	194
37-1	D5.1363.2	1064	*Lahillia*	13.5	9.2	–	149
36-1	D5.1359.2	1062	*Lahillia*	14.7	7.6	−4.3	75
35-1	D5.1355.2	1060	*Lahillia*	14.2	6.9	−9.6	117
34-1	D5.1351.2	1058	*Lahillia*	57.7	16.9	−17	109
33-1	D5.1343.2	1054	*Lahillia*	29.8	10.4	−6.5	109
32-1	D5.1339.2	1052	*Lahillia*	35.8	–	−8.8	272
30-1	D5.1336.2	1049	*Lahillia*	12.6	–	–	80
29-1	D5.1334.2	1047	*Lahillia*	0.7	−1.4	−2.2	528
24-1	D5.1313.2	1022–1028	*Lahillia*	9.2	5.3	−4.6	301
23-1	D5.1307.2	1019	*Lahillia*	19.4	–	−8.1	91
22-1	D5.1301.2	1010–1016	*Lahillia*	17.7	8.5	0.4	75
21-1	D5.1295.2	1007–1010	*Pycnodonte*	18.2	9.6	6.1	1402
20-1	D5.1289.2	1004	*Lahillia*	−10.7	−0.6	−11.6	24,319
18-1	D5.1277.2	986–992	*Pycnodonte*	17.8	8.5	−3.3	1109
16-1	D5.1270.2	980–986	*Pycnodonte*	18.4	10.3	−10.1	592
15-1	D5.1251.2	978–984	*Pycnodonte*	18.8	9.9	3.1	1232
14-1	D5.1248.2	972–978	*Pycnodonte*	17.0	9.4	7.5	578
13-1	D5.1245.2	966–972	*Pycnodonte*	17.80	10.3	−10.6	1472
12-1	D5.1241.2	960–966	*Pycnodonte*	17.0	8.4	15.0	1047
11-1	D5.1238.2	954–960	*Pycnodonte*	17.6	8.8	−5.5	1407
10-1	D5.1236.2	956	*Pycnodonte*	16.8	9.5	−0.2	370
9-1	D5.1234.2	948–954	*Pycnodonte*	18.3	9.4	13.8	1135
8-1	D5.1229.2	942–948	*Pycnodonte*	17.4	8.4	8.0	842
5-1	D5.1220.2	924–930	*Pycnodonte*	17.5	8.6	−3.5	1081
4-1	D5.1217.2	918–924	*Lahillia*	18.4	10.1	13.1	2342
3-1	D5.1214.2	912–918	*Lahillia*	17.9	10	17.1	1714
22-2	D5.1197.2	882–888	*Pycnodonte*	16.3	12.8	−0.5	659
19-2	D5.1138.2	772–778	*Cucullaea*	15.2	–	–	156.25
18-2	D5.1111.2	726–731	*Eselaevitrigonia*	16.0	11.0	–	282.27
16-2	D5.1040.2	656–661	*Cucullaea*	−5.16	6.9	−28.2	1058.61
15-2	D5.1021.2	636–641	*Cucullaea*	11.9	–	−11.7	128.42
14-2	D5.1006.2	621–626	*Pycnodonte*	18.0	12.1	−16.7	1811.69
13-2	D5.696.2	607–612	*Cucullaea*	16.2	–	–	44.98
12-2	D5.672.2	582–587	*Cucullaea*	18.1	12.1	−4.3	140.63
11-2	D5.370.2	549	*Pycnodonte*	18.0	10.2	−1.4	2134.57
9b-2	D5.347.2	522–527	*Leionucula*	5.4	–	−23.9	69.54
7-2	D5.970.2	442–447	*Oistotrigonia*	−2.9	4.1	−13.1	652.06
6-2	D5.955.2	427–434	Cucullaeidae	15.8	11.3	−1.0	92.50
2-2	D5.490.2	166	*Pycnodonte*	16.7	11	−2.5	767.90

CAS yield. The weight of the NaOCl- and CAS-$BaSO_4$ precipitates was corrected using the weight percent sulfur derived during isotopic analysis. Subsamples of the CAS-$BaSO_4$ precipitate powders were analysed for sulfur and oxygen isotope composition.

3.2. CAS ^{34}S and CAS ^{18}O isotope analysis

Sulfate isotopic analyses were performed on a Micromass Isoprime continuous flow mass spectrometer coupled to a Eurovector Elemental Analyser. $BaSO_4$ was weighed out in tin cups and converted to SO_2 by flash combustion at 1020 °C in the presence of oxygen. Excess oxygen was removed by reaction with copper wire at 650 °C and the SO_2 separated from other impurities using a chromatographic column and a helium carrier gas. The $\delta^{34}S$ of the sample is derived from the integrated mass 66 and 64 signals from the pulse of sample SO_2, compared to those in an independently introduced pulse of reference gas. These ratios were then calibrated using an internal seawater derived barium sulfate standard (SWS-3B) (+20.3‰) and CP-1, a chalcopyrite inter-laboratory standard (−4.56‰). The value for SWS-3B was calibrated using international standards (NBS-127 (+20.3‰), IAEA-S1 (−0.30‰), NBS-123 (+17.01‰), IAEA-s3 (−32.06‰) to the Vienna-Canyon Diablo Troilite (V-CDT) scale in per mille notation (‰). The precision obtained for repeat analysis of all laboratory standard materials and samples is better than ±0.3‰ (1 standard deviation).

The isotopic composition of the oxygen in the sulfate ion was measured by mixing $BaSO_4$ precipitates with spectroscopically pure graphite and placing the resulting mixture on platinum foils. These were then degassed and conductively heated under vacuum to about 1100 °C. A quantitative yield of CO_2 was achieved by converting any CO to CO_2 using a high voltage applied across platinum electrodes, whilst water was removed cryogenically. The $^{18}O/^{16}O$ ratios were measured on the CO_2 gas using VG SIRA 10 dual inlet, 90° magnetic sector gas source mass spectrometer and calibrated to the Vienna-Standard Mean Ocean Water (V-SMOW) scale using an internal standard (SWS-3B) calibrated to the V-SMOW scale using the international standard NBS-127 (+9.3‰). The precision obtained for all sulfate-O isotope measurements is 0.5‰ (1 standard deviation).

3.3. Carbonate carbon and oxygen isotopes ($\delta^{13}C_{carb}$, $\delta^{18}O_{carb}$), trace element (ICP-MS), and XRD analyses

Powdered shell material from all 58 samples used in CAS extraction were analysed for their bulk stable carbonate oxygen and carbon isotope compositions using a Micromass Multicarb Sample Preparation System attached to a VG SIRA Mass Spectrometer at the Godwin Laboratory, University of Cambridge. Each run of samples was accompanied by 10 reference carbonates and 2 control samples. The results are reported with reference to the international standard Vienna Pee Dee Belemnite (VPDB). The precision on repeat measurements is better than ±0.06‰ for $\delta^{13}C$ and ±0.08‰ for $\delta^{18}O$.

Shell powders were also analysed for their trace element content (Mg, Ca, Sr, Mn, Fe) in the labs of the National Oceanographic Center, Southampton. 2 mg of carbonate was dissolved in 20 ml of 3% HNO_3 containing 20 ppb Be and 5 ppb In and Re, with the addition of 10 µl of concentrated sub-boiled HNO_3. This solution was analysed on a ThermoFisher XSeries2 ICP-MS calibrated using synthetic standards also made up in 3% HNO_3 containing In, Re and Be at the same concentration to act as internal standards.

For XRD analyses, the powdered samples were front loaded into apertured low background silicon holders. The samples were analysed at the University of Leeds with a Bruker D8 using Cu Kα1 radiation, a Germanium primary monochromator and a Lynx Eye detector. All the samples were scanned at 40 kV, 40 mA from 2–86°, with an increment of 0.0105° and a count time of 2 s/step. The data were analysed using the Bruker's EVA for phase identification and TOPAS Rietveld refinement for phase quantification.

3.4. Cathodoluminescence and scanning electron microscopy

Shell material from total of seven specimens was cut and polished into thin sections using standard techniques, these were then examined visually on a cold cathode cathodoluminescence system (CITL 8200 Mk 3A mounted on a Nikon Optiphot petrological microscope) at the University of Edinburgh to identify areas of recrystallized carbonate. The same samples were also analysed using an FEI Quanta 650 scanning electron microscope (SEM) at the University of Leeds, operating in both back-scatter and secondary electron mode to identify original shell structure and contaminant sulfide minerals.

4. RESULTS

4.1. Sulfur isotopes: $\delta^{34}S_{CAS}$, $\delta^{18}O$ CAS, $\delta^{34}S_{hypochlorite\text{-}S}$, CAS-S and $\delta^{34}S_{hypochlorite\text{-}S}$ concentrations

Overall $\delta^{34}S_{CAS}$ values show significant variation, ranging from −10.7‰ to +57.7‰ with a mean of +16.1‰. As expected for biogenic samples, CAS-S concentration data are high (Staudt and Schoonen, 1995). These range from 45 pm to 24318 ppm with an average of 1241 ppm. Taxa which secreted a shell originally made of calcite (*Pycnodonte*) generally have substantially higher concentrations (averaging 1103 ppm) than those taxa with a primary aragonite shell (*Lahillia*, *Cucullaea*, *Eselaevitrigonia*) (averaging 421 ppm) (Table 1). The $\delta^{18}O$ CAS ranges from −1.4‰ to +16.9‰, with a mean of +9.01‰, while $\delta^{34}S_{hypochlorite\text{-}S}$ values range from −28.2‰ to +17.1‰ with an average of −3.55‰ (Fig. 2). Despite these broad ranges, much of the CAS dataset overlaps with published records of ocean sulfate-$\delta^{34}S$ for the late Cretaceous and Paleogene (Paytan et al., 1998; Paytan et al., 2004; Kampschulte and Strauss, 2004; Turchyn and Schrag, 2006).

4.2. Carbonate $\delta^{13}C$ and $\delta^{18}O$, trace element concentration

The preservation of a primary CAS signal is likely to be related to the preservation of primary biogenic carbonate. Both carbonate isotopes and trace element compositions of carbonate have been shown to be sensitive to diagenesis and have therefore been analysed to assess preservation of the CAS isotope signal. Bulk fossil shell powders yielded variable $\delta^{13}C_{carb}$ (range −7.19‰ to +4.13‰, average +0.82‰) and $\delta^{18}O_{carb}$ (range −0.58‰ to 2.15‰, average +0.78‰) values and highly variable trace element concentrations (Supplementary Information Table S2) (Fig. 3). These data are nevertheless within the range of previously published datasets using molluscan carbonate from the López de Bertodano Formation on Seymour Island (McArthur et al., 1998; Tobin et al., 2012; Tobin and Ward, 2015), and underlying formations in the James Ross Basin (Pirrie and Marshall, 1990; Ditchfield et al., 1994; Crame et al., 1999).

4.3. SEM, cathodoluminescence, XRD

Examination using SEM and cathodoluminescence of thin sections of bivalve shell material revealed most shell

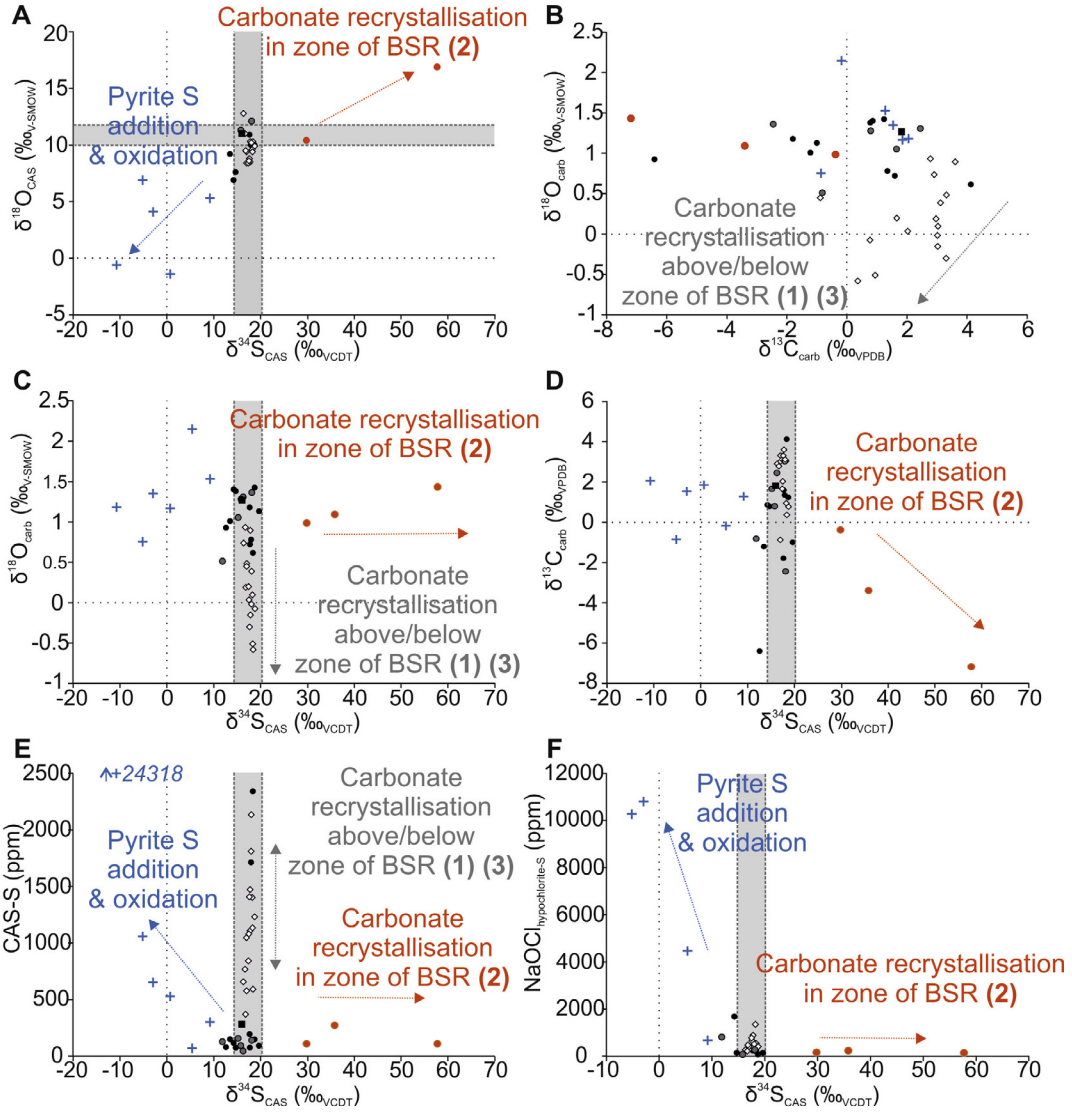

Fig. 3. Cross-plots of isotope data for the full CAS dataset for all species. A: $\delta^{34}S_{CAS}$ versus $\delta^{18}O_{CAS}$, B: $\delta^{13}C_{carb}$ versus $\delta^{18}O_{carb}$, C: $\delta^{34}S_{CAS}$ vs $\delta^{18}O_{carb}$, D: $\delta^{34}S_{CAS}$ versus $\delta^{13}C_{carb}$, E: $\delta^{34}S_{CAS}$ versus CAS concentration (ppm), F: $\delta^{34}S_{CAS}$ versus $\delta^{34}S_{hypochrlorite\text{-}S}$ concentration. Grey boxes in A, C, D, E, and F illustrate range of published Cretaceous–Paleogene seawater $\delta^{34}S$ and $\delta^{18}O$-S values (Claypool et al., 1980; Paytan et al., 1998; Paytan et al., 2004; Turchyn and Schrag, 2006). Filled black and red circles, *Lahillia*, filled grey circles, *Cucullaea*, filled white diamonds, *Pycnodonte*, filled black square *Eselaevitrigonia*. Numbers in parentheses represent possible zones of recrystallization in Fig. 5, with arrows indicating direction of change expected in isotope data. Blue crosses represent samples from a range of genera, likely contaminated with light sulfur from oxidation of sulfide minerals. (For interpretation of the references to colour in this figure legend, the reader is referred to the web version of this article.)

carbonate shows excellent preservation. Most samples were generally non-luminescent and with original shell microstructure preserved (Fig. 4). Exceptions included examples of contaminant minerals inside micro-borings or natural tubules in the shell, and luminescent cements within the shell material of many *Pycnodonte* oysters. XRD analysis confirmed the primary carbonate mineralogy of all taxa, while quantification of the percentage of various polymorphs (e.g. % calcite vs. aragonite) can be used to assess the preservation of shell material (see Section 5.2).

5. PRESERVATION AND ASSESSMENT OF A PRIMARY SEAWATER ISOTOPIC SIGNAL FROM CAS

A variety of studies on the durability and reliability of CAS indicate that alteration of the primary isotopic signal can occur as both an enrichment or depletion of $\delta^{34}S$ relative to known contemporaneous seawater values, and that such alteration can be the result of multiple processes (e.g. Lyons et al., 2004; Marenco et al., 2008a, 2008b; Gill et al., 2008; Newton et al., 2011; Rennie and Turchyn, 2014). However, most existing studies focus either on bulk CAS records from ancient and modern limestones or deep-sea carbonate oozes, or are derived from biogenic carbonates secreted by extinct groups of organisms (e.g. belemnites). Here we examine biogenic carbonates from thick-shelled marine bivalves of differing mineralogies. To test the validity of this dataset, a range of screening techniques were applied to the sample suite to distinguish primary isotope values (Figs. 4 and 5).

5.1. Oxidation of contaminant sulfide minerals

Although the CAS extraction is completed under anaerobic conditions, oxidation of contaminant sulfides within the sample is still possible during extraction. Carbonate powders were subject to NaOCl bleaching pre-treatment to remove organic sulfur, amorphous monosulfides, and potentially some sulfide minerals (see Wotte et al. (2012) for a detailed discussion). However, fine-grained sulfide-mineral grains can be wholly encapsulated by larger carbonate grains, shielding them from potential removal via the bleaching pre-treatment. Anaerobic oxidation is also possible via dissolved oxidised metal species released during extraction (Mazumdar et al., 2008). The sulfur added from sulfide minerals is derived from sulfide produced during MSR or sulfate-driven anaerobic oxidation of methane

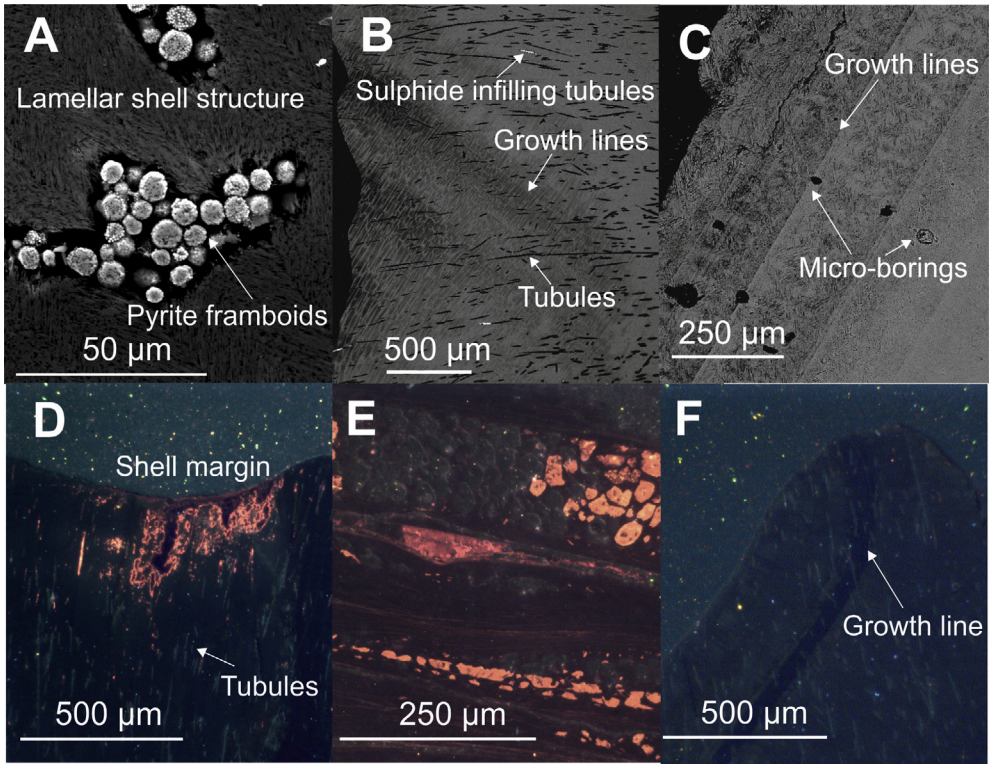

Fig. 4. Examples of shell preservation from fossil bivalve samples of the López de Bertodano Formation. Taken from SEM (A–C) and CL (D–F) imaging of fossil shells. A, (sample D5.1355.2, *Lahillia*) original pristine crossed-lamellar shell structure, with pyrite framboids inside micro-boring. B, (sample D5.955.2, *Cucullaea*) well-preserved shell structure including growth lines and tubules, some infilled with small amounts of sulfide (pyrite framboids). C, (sample D5.1355.2, *Lahillia*) further examples of lamellar shell structure, with growth lines and algal micro-borings into shell. D, (D5.955.2, *Cucullaea*) shell margin with non-luminescent primary shell structure, thin external layer showing a degree of luminescence and alteration possibly representing the remains of a periostracum. E, (D5.1277.2, *Pycnodonte*) showing generally non-luminescent shell with typical laminated and vesicular texture and areas in-filled with high magnesium luminescent calcite cements. F, (D5.955.2, *Cucullaea*) shell margin with well-preserved (non-luminescent) shell material and original growth lines.

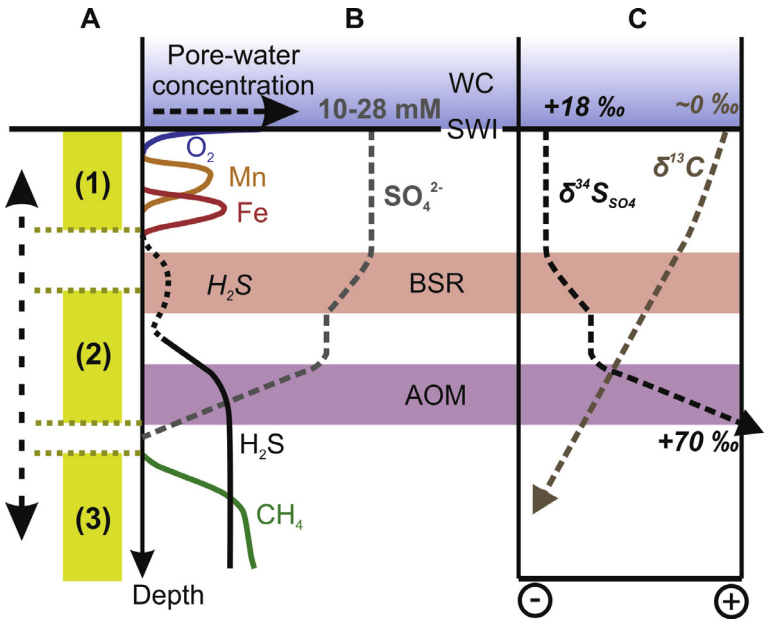

Fig. 5. Schematic pore water profile (not to scale). A: potential zones of alteration for fossil samples following burial and diagenesis. B: pore water concentration for various ions used as electron acceptors, and the concentration of sulfate. C: effect on the isotopic composition of sulfate ($\delta^{34}S_{SO4}$) and dissolved inorganic carbon ($\delta^{13}C$). MSR, microbial sulfate reduction, AOM, anaerobic oxidation of methane, WC, water column, SWI, sediment-water interface. Vertical dashed arrow next to A indicates the potential for these zones to migrate vertically through time due to a variety of factors. Modified from Jørgensen, and Kasten (2006).

(AOM) (Jørgensen and Kasten, 2006) in anoxic sedimentary pore waters. Since this is generally depleted in ^{34}S relative to seawater sulfate, the isotopic effect of this process is to decrease the apparent $\delta^{34}S$ of CAS as well as increasing the apparent CAS concentration (e.g. Marenco et al., 2008a; Mazumdar et al., 2008 Fike et al., 2015) (Fig. 3).

The oxidation of sulfide minerals during extraction will also effect the oxygen isotope composition of the sulfate. Leeds laboratory de-ionised water has a $\delta^{18}O_{V\text{-}SMOW}$ value of around −7‰. Incorporation of this water oxygen during oxidation of sulfide minerals to sulfate will therefore also lead to a depletion in $\delta^{18}O_{CAS}$. SEM examination of several shells (6-2, 12-1, 18-1, 35-1) in the total dataset revealed that pyrite framboids are present within the infill of micro-borings or natural tubules in shell structure of the genera *Lahillia* and *Cucullaea* which otherwise preserve pristine original shell microstructure and are non-luminescent during examination under CL (Fig. 4). Since pyrite emplacement in shell material can occur in pre-existing natural voids in the shell structure (such as tubules or borings) (Fig. 4A and B), measures of carbonate preservation (e.g. cross-plots of $\delta^{18}O_{carb}$ and $\delta^{13}C_{carb}$, and trace element composition) are not relevant when assessing this process and should show no distinct correlation as contamination can occur with no effect on the structure and composition of shell carbonate.

A total of six fossil samples (four Maastrichtian (7-2, 9-2, 16-2, 20-1) and two Danian (24-1, 29-1)) record $\delta^{34}S_{CAS}$ values significantly depleted relative to the overall trend of the remaining dataset and of contemporaneous published seawater values (e.g. Paytan et al., 1998; Paytan et al., 2004; Kampschulte and Strauss, 2004; Turchyn and Schrag, 2006) (Fig. 3A, C, D, E, and F). In addition, these samples also record negative $\delta^{18}O_{CAS}$ and $\delta^{34}S_{hypochlorite\text{-}S}$ values (Fig. 2), and elevated concentrations of non-CAS-S (represented by hypochlorite-S ppm values) although other measures of carbonate preservation suggest they are well preserved (Fig. 3B). Correlation of these variables alone indicates these samples are likely not recording a seawater signature. Measurement of the isotopic composition of sulfur removed by the sodium hypochlorite bleach in these samples (range +17.1‰ to −17‰, mean of −1.47‰) indicates that the sum of sulfide plus organic sulfur in these samples broadly conform to the hypothesised addition of isotopically depleted sulfide via partial oxidation of organic sulfur and/or pyrite sulfur, although this is likely an estimate rather than a perfectly quantified measurement of possible contamination as NaOCl bleaching may only ever partially remove pyrite-S (Wotte et al., 2012). An additional sample (15-2) exhibits a low $\delta^{34}S_{CAS}$ value (+11.86‰) compared to stratigraphically adjacent samples (Fig. 2). This sample also has quite a negative $\delta^{34}S_{hypochlorite\text{-}S}$ value (−11.7‰), indicating that some addition of light sulfur is possible. Against this hypothesis, it exhibits low CAS concentration, and ultimately lacks confirmation as an $\delta^{18}O_{CAS}$ value could not be obtained. It is included in the final dataset with these caveats.

These data suggest that pyrite addition is variable, and that the sum of contaminent S-phases in fossil samples themselves (as represented by the $\delta^{34}S_{hypochlorite\text{-}S}$) clearly has a variable isotope composition. Therefore, the potential for alteration of the primary CAS isotope signal is also variable at the level of each individual shell. In only a few examples oxidation of sulfides has occurred – perhaps because of

the failure to remove monosulfides or organic sulfur during sample bleaching, or pyrite oxidation during sample extraction. Due to the high probability of contamination, the six datapoints described above are removed from subsequent analysis and discussion of the primary record.

5.2. Recrystallisation following shallow marine diagenesis

A second suite of processes linked directly to the preservation or alteration of original carbonate material during diagenesis also have the potential to alter the CAS from a primary seawater isotope composition. Data from several samples are consistent with at least partial recrystallisation of original shell material (Fig. 3) or the incorporation of later diagenetic cement into their shell microstructure (Fig. 4). However, the degree to which these processes may have affected CAS values in these shells depends largely on the relative timing of diagenetic alteration following death and burial in the sediment column. The influence of local pore water chemistry and biogeochemical processes in driving changes to sulfur cycle proxies such as biogenic CAS should be considered before any deep-time record is interpreted to represent a true picture of seawater chemistry. To explore the effects of these processes, a conceptual model based around a pore-water profile with typical biogeochemical zonation seen in marine sediments during the breakdown of organic matter (Jørgensen and Kasten, 2006) is used to consider the likely effect of recrystallisation on CAS, carbonate carbon and oxygen isotope, and trace element values in three hypothetical 'zones of alteration' following burial (Fig. 5):

1. Shallow zone with concentrations of sulfate near seawater. Here porewater sulfate isotope compositions will also be near those of seawater, but concentrations of iron and manganese are likely to be elevated. Incorporation of sulfate into recrystalised carbonate here will not result in any significant deviation from a primary signal.
2. Intermediate depth zone with depleted porewater sulfate concentrations relative to seawater. The porewater sulfate has a more positive sulfur isotope composition than seawater due to MSR and/or AOM. Here, sulfate concentrations are still sufficient to produce a significant concentration of CAS in recrystalised carbonate, but addition of recrystallised carbonate will now shift the CAS-S isotope composition towards heavier values. The isotopic composition of dissolved inorganic carbon (DIC) becomes increasingly more negative for both carbon and oxygen in this zone.
3. Deep zone where sulfate concentrations are negligible. Recrystallisation here has a minimal effect on CAS sulfur isotope compositions because the new carbonate will contain little or no sulfate. The carbon and oxygen isotope compositions of DIC are shifted to more negative values here.

The zone of recrystallization of carbonate is likely to vary depending on carbonate mineralogy and sedimentation rate. Rennie and Turchyn (2014) suggested a relationship between CAS alteration and sedimentation rate; such that preservation of primary $\delta^{34}S_{CAS}$ values was more likely in sites with low sedimentation rates, where recrystallization would occur above a deeper zone containing isotopically evolved pore fluids (Zone 1 of Fig. 5), or in settings with very high sedimentation rates where samples would be rapidly placed below this critical region before recrystallization could occur (e.g. into Zone 3 of Fig. 5). CAS was thus most prone to alteration at intermediate sedimentation rates – estimated at 50–150 m Myr^{-1}, which would be comparable to estimates for the López de Bertodano Formation on Seymour Island (100–150 m Myr^{-1} based on average calculated sedimentation rate for the entire 1100 m-thick succession) (Tobin et al., 2012; Bowman et al., 2013; Witts et al., 2016) The presence of glauconite-rich horizons in the uppermost ~300 m of the López de Bertodano Formation indicate intervals of significantly lower sedimentation rate and reworking of sediment (Macellari, 1988; Witts et al., 2016), whilst the more mud-rich parts of the succession were likely deposited under even higher sedimentation rates than the calculated average.

Application of this general model to the present study should also be approached with caution given the differing palaeoenvironmental setting. In deep sea carbonate dominated sediments, such as those studied by Rennie and Turchyn (2014), high rates of carbonate recrystallization occur at shallow depths in the sediment column in association with pore waters containing relatively unevolved $\delta^{34}S_{SO4}$, whereas the zones of MSR and AOM may be >1 m (and in some cases, tens of meters) below the sediment-water interface (Rennie and Turchyn, 2014; Turchyn et al., 2016).

In shallower water settings, such as those considered in this study, the zones of MSR and AOM may occur a lot closer (mm to cm-scale for MSR, cm to m-scale for AOM) to the surface (e.g. Jorgensen, 1982; Jorgensen and Kasten, 2006; Rooze et al., 2016) potentially in association with higher rates of recrystallization. Biogeochemical zones are also likely to migrate over time with changes in sedimentation rate, organic matter delivery, or concentration of ions diffusing from the overlying water column (Fig. 5), making relationships with sedimentation rate more complicated. Finally, samples of biogenic carbonate from thick-shelled marine bivalves are also substantially different to those from deep sea foraminiferal oozes since they have a much lower surface area to volume ratio. Our data also indicate that calcitic taxa such as *Pycnodonte* oysters start with an initially higher CAS concentration than foraminifera and aragonitic taxa and are therefore less vulnerable to alteration. Aragonitic taxa have the advantage that their progressive recrystallisation can be monitored by the percentage of calcite in their shell (see below).

Turning to the primary dataset presented herein, many specimens of *Pycnodonte*, which originally secrete a calcite shell, contain significant enrichment in Mn and Fe and exhibit a relationship between decreasing values of $\delta^{18}O_{carb}$, $\delta^{13}C_{carb}$ and decreasing Sr content, as would be expected during progressive diagenetic recrystallization in Zone 1 (Fig. 6). Examination using cathodoluminescence and SEM revealed good preservation of original shell material (Fig. 4E), but that the 'layer cake' vesicular shell structure

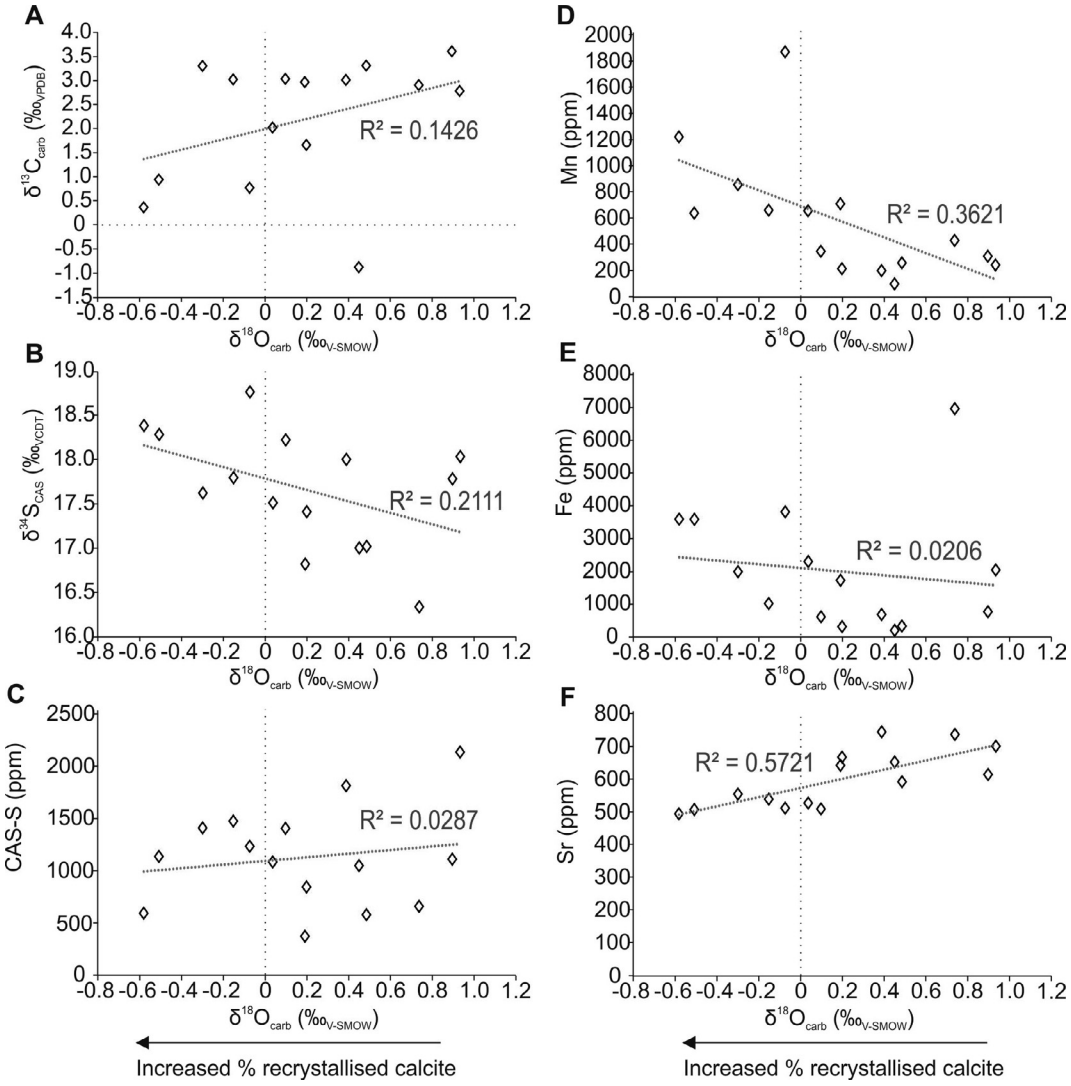

Fig. 6. Cross-plots between $\delta^{18}O_{carb}$ and A: $\delta^{13}C_{carb}$, B: $\delta^{34}S_{CAS}$, C: CAS-S ppm, D: Mn, E: Fe, F: Sr for calcitic *Pycnodonte* oysters. Significant correlations between decreasing $\delta^{18}O_{carb}$ and any of these variables is often interpreted as a sign of increasing recrystallization and loss of primary CAS isotope signal (e.g. Brand and Veizer, 1980; Gill et al., 2008).

tends to contain significant areas of luminescent, presumably early diagenetic cement. This has been noted by previous studies (Pirrie and Marshall, 1990; Ditchfield et al., 1994), and led to the suggestion of excluding *Pycnodonte* samples from paleotemperature reconstructions from the James Ross Basin using $\delta^{18}O_{carb}$. Importantly for this study, $\delta^{34}S_{CAS}$ and $\delta^{18}O_{CAS}$ values for all *Pycnodonte* samples are within the range of contemporaneous seawater (range 16.3–18.8‰ for $\delta^{34}S_{CAS}$, 8.4–12.8 for $\delta^{18}O_{CAS}$), and they exhibit high CAS-S concentrations (minimum 370 ppm, maximum 2134 ppm, average 1102 ppm), with no relationship between $\delta^{18}O_{carb}$ (Fig. 6C) and CAS concentration, and only a very weak relationship between $\delta^{18}O_{carb}$ (Fig. 6B) and $\delta^{34}S_{CAS}$. This strongly suggests that despite recrystallization, $\delta^{34}S_{CAS}$ values in these bivalves are buffered from alteration and likely record primary seawater values.

Taxa with primary aragonite shells (*Lahillia*, *Cucullaea*, *Eselaevitrigonia*) show mostly good visual preservation of original shell microstructure with little or no development of diagenetic cements (Fig. 4), indicating significant amounts of recrystallisation has likely not occurred in the majority of samples. Assessment of preservation for originally aragonite samples is important because it has been demonstrated that sulfate incorporation occurs more favourably in calcite than aragonite (Busenberg and Plummer, 1985). Compatible with this notion, these bivalves generally show lower or substantially more variable CAS-S concentrations than the calcitic *Pycnodonte* oysters (mean for aragonitic taxa 332 ppm, standard deviation, 609 ppm), suggesting that they are less buffered from the effects of diagenesis on their CAS record. Detailed examination of well-preserved specimens of *Lahillia* and *Cucullaea* also reveal that these taxa have an organic-rich outer layer, likely the remains of a periostracum. This layer appears prone to alteration and shows luminescence under CL imaging, suggesting it could contribute to at least

partial modification of the original shell material during early diagenesis (Fig. 4D). This outer layer can be removed or avoided during microsampling. The surface of the shell material used in this study was not cleaned in this way and this layer is therefore potentially included in the homogenised samples.

To assess the amount of recrystallization and potential alteration of CAS in originally aragonitic bivalves from the primary dataset, quantitative XRD was used to estimate the proportion of aragonite to calcite in each shell (Fig. 7), and compared to isotope values and trace element concentrations. Incorporation or contamination of shells with other minerals (i.e. sediment not removed during sample cleaning), could lead to anomalous trace element values, so estimates of the percentage of 'other' minerals included in the shells were also examined for most samples (Supplementary Information Table S2).

Cross-plots of these variables (Fig. 7) indicate that several samples of *Lahillia* in the dataset show varying degrees of alteration of the original aragonite shell to calcite, likely representative of early diagenetic recrystallisation. By contrast, *Cucullaea* samples are better preserved, showing minimal alteration to calcite, and negligible incorporation of contaminating minerals from the surrounding sediment. Sample 30-1 (*Lahillia*) shows a moderate degree of recrystallization (36.8% calcite) and records a $\delta^{34}S_{CAS}$ value that is lower than expected for Cretaceous seawater sulfate (Fig. 7A), but it is not different to stratigraphically adjacent samples (Fig. 2A – 1049 m). Sample 30-1 also shows evidence for enrichment in Fe and Mn, as would be expected from recrystallization in zone 1 (Fig. 5). Two samples (3-1 and 4-1 – both *Lahillia*) are highly recrystallized (65.5% and 98.3% calcite respectively), but record $\delta^{34}S_{CAS}$ values in the range of seawater values from other studies. They also have elevated CAS-S concentrations consistent with the addition of calcite with high sulfate concentrations relative to aragonite. These samples are also considered recrystallized in Zone 1, despite the lack of significant Fe and Mn enrichment.

Three samples (32-1, 33-1, 34-1 – all *Lahillia*) with very enriched $\delta^{34}S_{CAS}$ values flagged previously (Fig. 3) exhibit varying levels of recrystallization (26%, 16%, and 37% calcite respectively). This evidence of conversion from aragonite to calcite in conjunction with their elevated $\delta^{34}S_{CAS}$ values are perhaps indicative of recrystallization in Zone 2; in an interval where pore-waters concentrations and isotope compositions are modified by MSR or AOM. One of these samples (34-1), as well as a further *Lahillia* which records expected seawater $\delta^{34}S_{CAS}$ values (sample 38-1) show also elevated Mn and Fe values, as would be expected by recrystallization in Zone 1. However, both samples appear to be contaminated by incorporation of other minerals, probably because of failure to remove adhering sediment during cleaning or shell bleaching with NaOCl (Fig. 7H and J) which is likely to have elevated measurements of Fe and Mn.

To summarise this assessment of preservation, numerous specimens of *Lahillia* and *Cucullaea* show evidence consistent with at least partial diagenetic recrystallization of an originally aragonitic shell to calcite, while several originally calcitic *Pycnodonte* oysters show evidence for the addition of authigenic or diagenetic cements into the shell structure. Using a conceptual model to examine the likely signature of any such changes in terms of the isotopic composition of the shell material and trace element concentrations, aragonite samples that recrystallized in Zone 2 are removed from the final dataset due to their modified $\delta^{34}S_{CAS}$ values (Table 2), along with samples considered non-primary from pyrite-S addition. Remaining samples where there is no evidence of pyrite oxidation during extraction, no evidence of alteration to the primary shell carbonate, or where alteration to the shell carbonate has occurred in such a way as to preserve the primary seawater signal, are considered to represent a primary record of seawater sulfate (Fig. 8). These data are discussed in the next section.

6. DISCUSSION

6.1. Summary of sulfur-cycle changes across the Maastrichtian and early Danian in Antarctica

The $\delta^{34}S_{CAS}$ dataset remaining after screening for preservation is presented in Fig. 8 where temporal trends in $\delta^{34}S_{CAS}$ are apparent. These are interpreted to represent a true picture of the evolution of seawater sulfate during the Maastrichtian and early Danian. No directly compatible data are available in terms of the temporal resolution of this study, as existing datasets either focus on a narrow window around the K–Pg boundary interval itself (Kajiwara et al., 1992; Kaiho et al., 1999) or are long-term records derived from marine barite at low resolution and with major time gaps (Paytan et al., 1998; Paytan et al., 2004). These low-resolution records show a lack of fluctuation in the Maastrichtian, all data ranging between +18‰ and +19‰ (Paytan et al., 2004). Kampschulte and Strauss (2004) reported values from CAS for the 70–65 Ma time bin of between +18.1‰ and 18.6‰, and +16.9‰ to +17.4‰ from evaporates of the same age.

Broadly speaking, our primary CAS data are comparable with existing estimates of the isotopic composition of seawater sulfur for the Maastrichtian and Danian from published datasets (Fig. 9) (e.g. Kaiho et al., 1999; Paytan et al., 1998; Paytan et al., 2004), but add new detail, particularly in an interval spanning around 2 million years across the K–Pg boundary itself (the consecutive magnetochrons C30N and C29R) (Fig. 8).

The precision of CAS in recording seawater $\delta^{34}S$ means that variability is generally only considered significant when changes exceed >1‰ (Rennie and Turchyn, 2014). We therefore interpret the remaining record in terms of three main features (labelled 1–3 on Fig. 8):

(1) Early-mid Maastrichtian (magnetochron C31R) stability in the basal portion of the López de Bertodano Formation (100–600 m). Data density is low but $\delta^{34}S_{CAS}$ values average 17‰ ± 1‰, with values at the higher end of this range around 600 m, during the mid–Maastrichtian (~69 Ma, close to the base

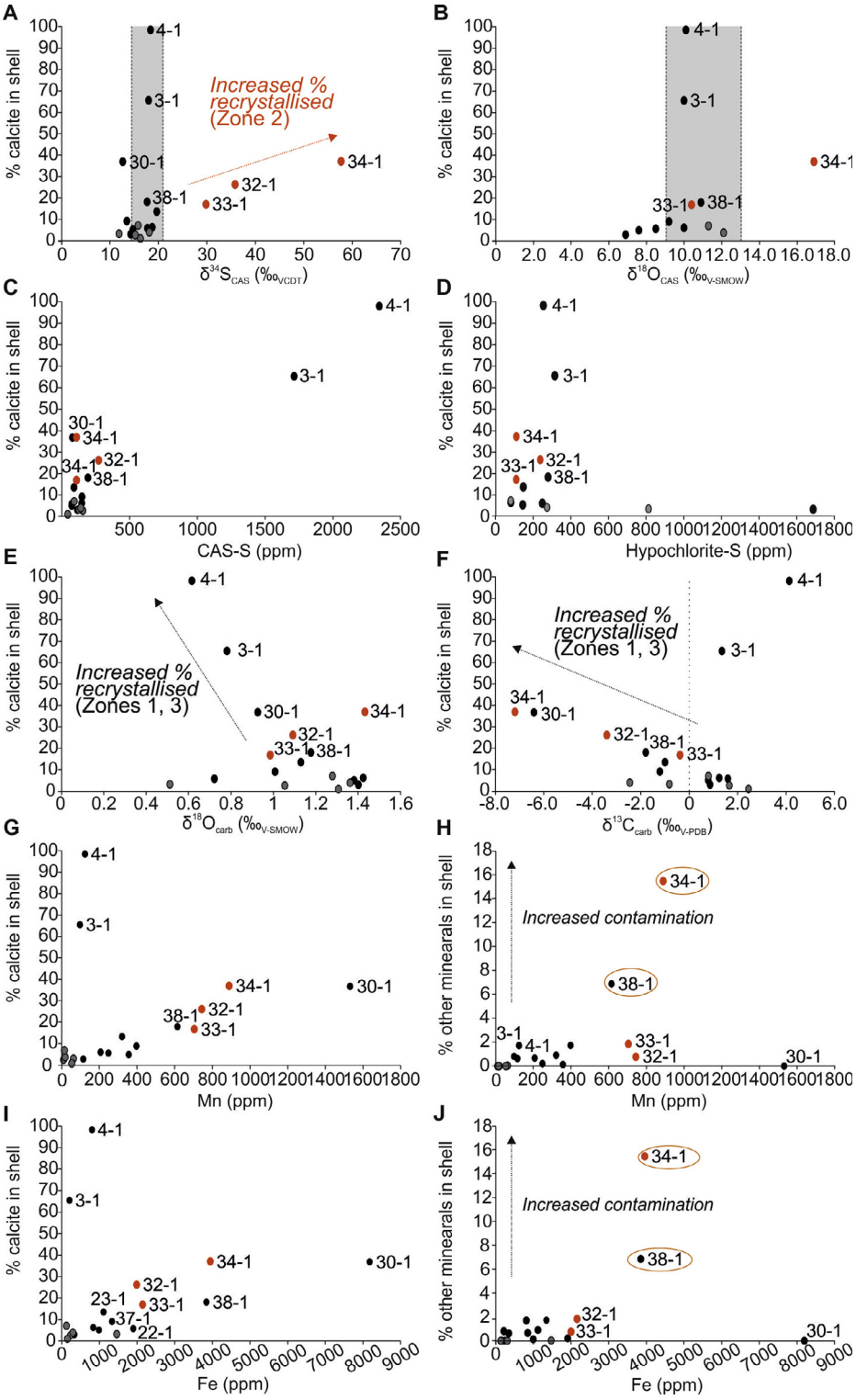

Fig. 7. Cross-plots for originally aragonite taxa (*Lahillia*, *Cucullaea*). Cross plots based on quantified XRD analysis between % calcite in shell (A, B, C, D, E, G, I) and A: $\delta^{34}S_{CAS}$, B: $\delta^{18}O_{CAS}$, C: CAS-S, D: Hypochlorite-S, E: $\delta^{18}O_{carb}$, F: $\delta^{13}C_{carb}$, G: Mn (ppm), I: Fe (ppm). H and J: % other (contaminating) minerals in shell and H: Mn (ppm) and J: Fe (ppm). Black and red circles represent *Lahillia*, grey circles *Cucullaea*. Samples numbers correspond to Table 1. Arrows represent direction of change expected during recrystallization or contamination in zones of alteration from Fig. 5. Grey bars on A and B are range of Cretaceous–Paleogene values of $\delta^{34}S_{CAS}$ and $\delta^{18}O_{CAS}$. (For interpretation of the references to colour in this figure legend, the reader is referred to the web version of this article.)

Table 2
List of CAS samples removed from final analysis following assessment of preservation.

Sample #	Strat height (m)	Reason for removal	$\delta^{34}S_{CAS}$
34-1 (D5.1351.2)	1058	Recrystalisation in Zone 2	+57.7‰
33-1 (D5.1343.2	1054	Recrystalisation in Zone 2	+29.8
32-1 (D5.1339.2)	1052	Recrystalisation in Zone 2	+35.8
29-1 (D5.1334.2)	1047	Pyrite-S addition	+0.7
24-1 (D5.1313.2)	1022–1028	Pyrite-S addition	+9.2
20-1 (D5.1298.2)	1004	Pyrite-S addition	−10.7
16-2 (D5.1040.2)	656–661	Pyrite-S addition	−5.2
9b-2 (D5.347.2)	522–527	Pyrite-S addition	+5.4
7-2 (D5.970.2)	442–447	Pyrite-S addition	−2.9

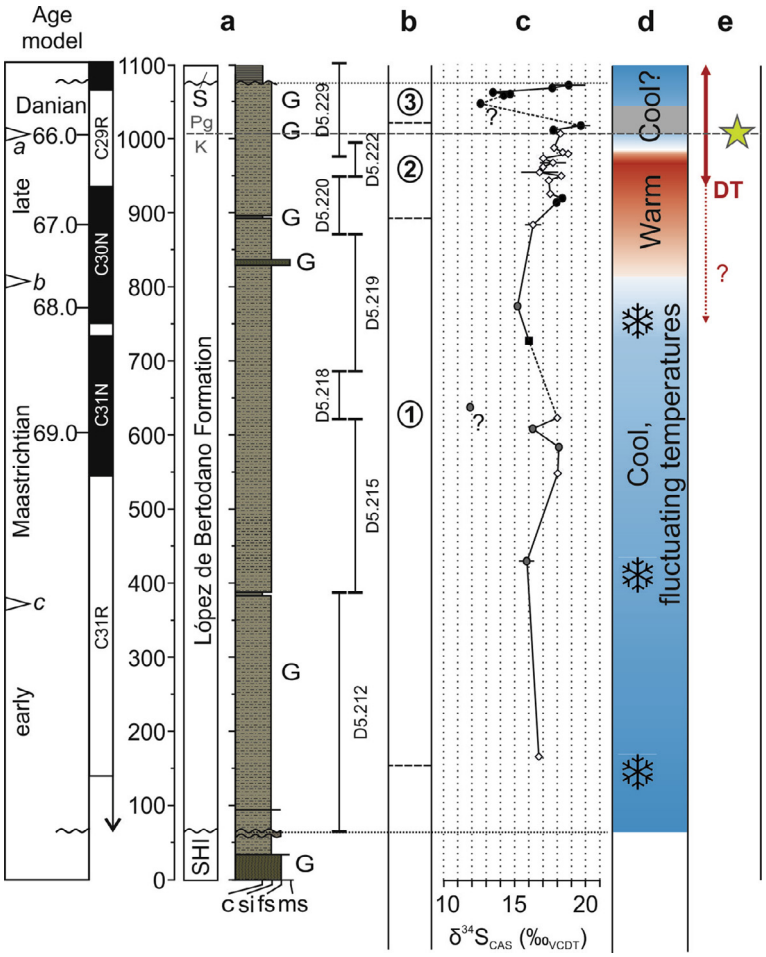

Fig. 8. a: Composite lithostratigraphy and age model for section D5.251. b: divisions of $\delta^{34}S_{CAS}$ dataset discussed in main text. c: Primary $\delta^{34}S_{CAS}$ dataset. For explanation of differing symbology relating to different taxa see Fig. 3. d: summary regional palaeoclimate interpretation. Data derived from carbonate oxygen isotopes (Tobin et al., 2012), marine (Bowman et al., 2013) and terrestrial (Bowman et al., 2014) palynology. Snowflake symbols are 'cold snaps' of Bowman et al. (2013). Grey bar extending from K–Pg boundary represents uncertainty in palynological climate proxy interpretation due to disruption of marine and terrestrial communities following the K–Pg mass extinction. e: Timing and evidence for LIP volcanism and impact events. Red arrow labelled DT is the inferred duration of the Deccan Traps LIP – solid red line marks timing of Main Phase eruptions (Schoene et al., 2015; Renne et al., 2015) dashed red line and ? mark timing of phase 1 (Chenet et al., 2009). The K–Pg boundary is represented by the dashed horizontal grey line at 1008 m (Bowman et al., 2012; Witts et al., 2016). Yellow star marks position of the iridium anomaly on Seymour Island in a parallel section (Elliot et al., 1994), taken as a global marker for the Chicxulub impact event (Molina et al., 2006). (For interpretation of the references to colour in this figure legend, the reader is referred to the web version of this article.)

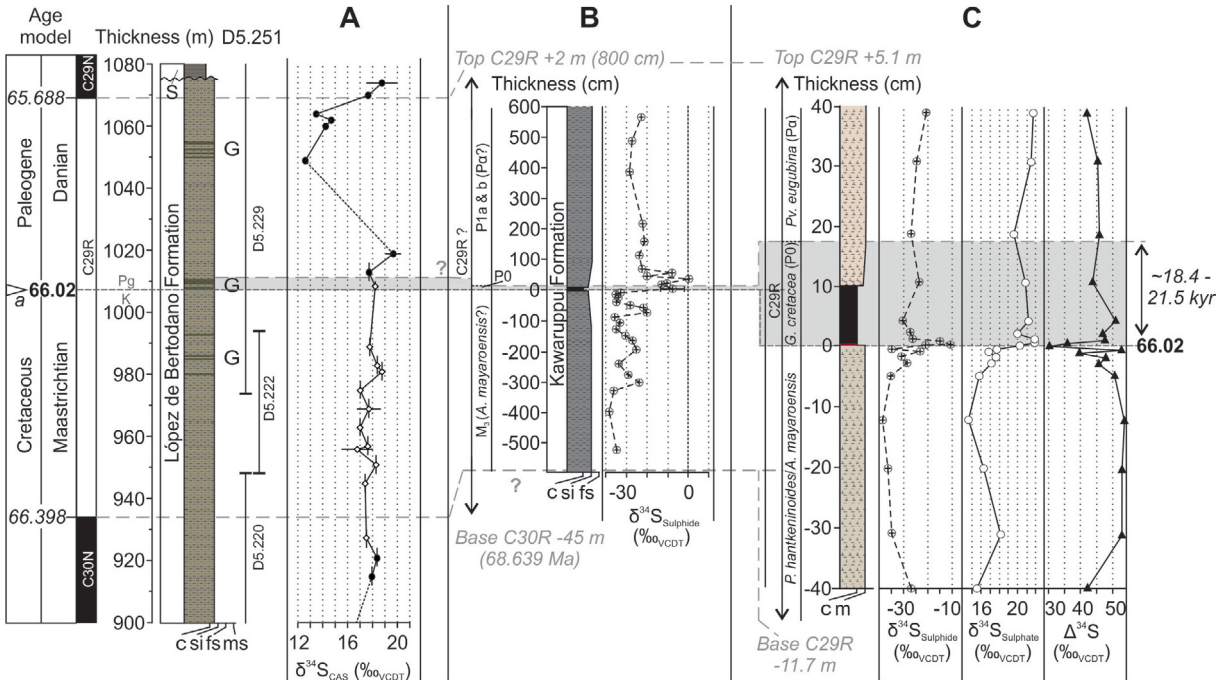

Fig. 9. Correlation and comparison of K–Pg sulfur isotope data from this study (A - Seymour Island, Antarctica - $\delta^{34}S_{CAS}$) with existing datasets from Kawaruppu, Japan (B) (Kajiwara and Kaiho, 1992) ($\delta^{34}S_{Sulfide}$) and Caravaca, Spain (C) (Kaiho et al., 1999) ($\delta^{34}S_{Sulfide}$, $\delta^{34}S_{Sulfate}$, $\Delta^{34}S$). Attempted correlation (horizontal dashed grey lines and shaded grey box) using age models. Primarily magnetostratigraphy (Arenillas et al., 2004 (Caravaca); Tobin et al., 2012 (Seymour Island); Kurihara et al., 2016 (Kawaruppu)) and biostratigraphy –estimates for the duration of the P0 foraminiferal biozone found in both the Kawaruppu (Kaiho and Saito, 1986) and Caravaca sections (Arenillas et al., 2004; Molina et al., 2009). Base of this biozone is the K–Pg boundary (Molina et al., 2006, 2009). Estimated correlation with Seymour Island based on sedimentation rates of 0.1–0.2 mm/yr (Tobin et al., 2012; Witts et al., 2016). Vertical error bars on $\delta^{34}S_{CAS}$ dataset in A represent stratigraphic sampling bins from which fossils were collected. Horizontal error bars represent range of multiple $\delta^{34}S_{CAS}$ values, with marker located at the mean value. Dashed line in the early Paleocene record represents absence of well-preserved CAS data. G, glauconite-rich horizons, also marked as green bands in lithostratigraphy of A. S, Sobral Formation. Expanded foraminiferal species names from biostratigraphy in B and C: *A. mayaroensis* = *Abathomphalus mayaroensis, P. hantkeninoides* = *Plummerita hantkeninoides*, *G. cretacea* = *Guembelitria cretacea*, *Pv. eugubina* = *Paravularugoglobigerina eugubina*. (For interpretation of the references to colour in this figure legend, the reader is referred to the web version of this article.)

of chron C31N). This interval finishes with slightly lower values (15–16.5‰) between 700 and 800 m, (corresponding to magnetochrons C30R and C30N and an age of ~68 Ma).

Environmental fluctuations preceding the K–Pg mass extinction include a long-term global cooling trend reaching its peak across the Campanian–Maastrichtian boundary and during the early Maastrichtian (Barrera and Savin, 1999; Friedrich et al., 2012; Bowman et al., 2014; Thibault, 2016) followed by further warming ~69 Ma (the 'Mid-Maastrichtian Event' (MME)) (Voigt et al., 2012; Jung et al., 2013). Large and apparently rapid sea level changes also occurred at this time, superimposed on an overall long-term fall from a mid-Cretaceous high (e.g. Miller et al., 2005; Haq, 2014). These environmental changes are associated with several biotic events – most notably the final extinction of the 'true' inoceramid bivalves during the mid-Maastrichtian (MacLeod et al., 1996; Dubicka and Peryt, 2012; Jung et al., 2013), following a protracted latitudinal decline which likely began in the southern high latitudes during the Campanian (Crame et al., 1996; Olivero, 2012).

Due to the low density of data in the portion of the CAS record that correlates with this time interval, it is difficult to test whether these global events had a significant effect on the sulfur cycle. The early Maastrichtian CAS record probably represents subtle fluctuations within a system close to steady state. A slight increase in $\delta^{34}S_{CAS}$ values between 400 and 600 m in the composite section could plausibly reflect increased global pyrite burial during the MME sea level rise and climate warming (Fig. 8), with burial of isotopically light pyrite-sulfur on a global scale leading to an enrichment in $\delta^{34}S$ of the oceanic reservoir. A positive shift in global carbon isotope records is also recorded during the MME, suggesting a period of increased carbon burial (Voigt et al., 2012).

(2) Late Maastrichtian increase (between 750–1020 m) from a low point of ~15.5‰ to 19.6‰ at 1019 m, ~10 m above the K–Pg boundary (corresponding to the upper portion of magnetochron C30N and lower

two thirds of C29R, 67–66 Ma). This feature occurs where data density is highest, although the most positive value above the K–Pg boundary is only recorded by one sample.

(3) An early Paleocene negative excursion and recovery from the peak positive value in the earliest Palaeocene to a cluster of depleted values defined by four datapoints (range 12.6–14.7‰, mean 13.8‰) occurring in stratigraphically adjacent samples between 1049 and 1064 m, 40 m above the K–Pg boundary (corresponding to the upper portion of chron C29R, ~65.7 Ma). The $\delta^{34}S_{CAS}$ values then return to values of 17–19‰, like those of the late Maastrichtian in the highest portion of the section (1070–1074 m), directly below the unconformable contact with the overlying Sobral Formation.

6.1.1. Late Maastrichtian increase in $\delta^{34}S_{CAS}$ – potential environmental causes

An increase in $\delta^{34}S_{CAS}$ of ~4–5‰, from magnetochron C30N, to a maximum just above the K–Pg boundary is well constrained by multiple data points, and represents a true shift in the isotopic value of seawater sulfate during this time interval. Despite this, the effect of climate or sea level on the $\delta^{34}S_{CAS}$ values during the late Maastrichtian is not easily linked to a known change in global climate or tectonics. The major positive shift in the CAS record from Seymour Island begins in magnetochron C30N (Figs. 8 and 9), an interval where most climate proxies globally show evidence for significant cooling (e.g. Li and Keller, 1998; Thibault, 2016). Although the global sea level record for this interval lacks precise temporal constraints, it is broadly characterised by a rise in C30N followed by a fall into C29R (Miller et al., 2005; Haq, 2014), at odds with a role in controlling a persistent increase in pyrite burial.

Because of the tight coupling apparent in marine sediments between the burial of isotopically depleted organic-carbon and pyrite-sulfur, any increase in pyrite burial, indicated by a significant positive shift in the sulfur isotope record, should be mirrored by an increase in carbon burial (Berner, 1982). If this is large enough it will impact on the isotopic composition of ocean DIC and be recorded in the record of marine carbonates. Numerous carbon isotope curves derived from bulk carbonate (e.g. Voigt et al., 2012; Thibault, 2016) or foraminifera (Li and Keller, 1998) are available for the Maastrichtian from a variety of ocean basins (Wendler, 2013). They generally show a long-term decreasing trend of only around 0.8–1‰ magnitude in the late Maastrichtian, followed by a short and rapid positive peak immediately preceding the K–Pg boundary (Cramer et al., 2009; Voigt et al., 2012). Several of these records come from epeiric seas which have the potential to record an isotopic composition different to the global ocean (e.g. Panchuk et al., 2006; Voigt et al., 2012). Despite this, few carbon isotope records show any significant (>1‰) increase prior to this during the late Maastrichtian, as might be expected during a period of increased linked carbon and pyrite burial inferred from the increase in $\delta^{34}S_{CAS}$ values during magnetochrons C30N–29R.

There are several possibilities to explain this apparent contradiction; a decoupling of the carbon and sulfur cycles via terrestrial carbon cycle changes (e.g. Kurtz et al., 2003), or a reduced significance of marine sulfate-sulfur isotopic change for the carbon cycle due to lower marine sulfate concentrations. Decoupling has been hypothesised for the early Paleogene (Kurtz et al., 2003) with a decrease in pyrite burial coinciding with an increase in terrestrial organic carbon burial. Hence increases in marine organic carbon burial may be balanced by decreases in terrestrial organic-carbon burial such that the net effect on the DIC-carbon isotope composition of the ocean is only small. There is also evidence for reduced concentrations of sulfate in the late Cretaceous oceans (Wortmann and Paytan, 2012; Holt et al., 2014). A lower marine sulfate concentration would make the marine sulfate sulfur more sensitive to change for any given amount of carbon/pyrite burial. Therefore, there could be sufficient pyrite burial to impact the CAS record significantly whilst having only a minimal effect on the isotopic composition of ocean DIC. Changes in the extent and burial rate of organic matter in anoxic or euxinic basins, where carbon and sulfur can be buried in differing proportions (Raiswell and Berner, 1985), could also have played a role. There is however, limited evidence for any significant expansion of such settings globally during the Maastrichtian.

Large-scale volcanism has also been suggested as a driver of change in the Cretaceous sulfur cycle (Paytan et al., 2004; Adams et al., 2010; Gomes and Hurtgen, 2016). As well as causing or exacerbating climate-driven changes, LIP volcanism could contribute significant amounts of volcanic or mantle sulfur (isotopic composition of 0‰) to the ocean (e.g. Adams et al., 2010; Gomes and Hurtgen, 2016), causing a decrease in $\delta^{34}S$. Extensive continental flood basalt volcanism from the Deccan Traps LIP in India commenced ~1.2 myrs prior to the K–Pg boundary (Chenet et al., 2009), with the main phase of eruptions (accounting for ~80% of the total eruptive volume) confined to a 750 kyr interval in the latest Maastrichtian and early Danian, with a peak in eruptive activity occurring in magnetochron C29R close to the K–Pg boundary (Robinson et al., 2009; Schoene et al., 2015; Renne et al., 2015). An estimated $>1.3 \times 10^6$ km^3 of lava was erupted from the Deccan Traps, with total volatile emissions generally thought to be high compared to other LIPs (totals of $3.5–6.5 \times 10^6$ Mt SO_2, 1.4×10^7 Mt CO_2, and 1×10^6 Mt Cl respectively) (Self et al., 2014). Individual eruptions probably occurred as short-lived pulses, and Callegaro et al. (2014) suggested that each 1 km^3 of Deccan lava erupted would outgas 8 Mt of SO_2. The potential for environmental change resulting from release of these volatiles is still debated (Schmidt et al., 2016; Tobin et al., 2017).

The lack of significant excursions in the CAS record during the stratigraphic interval correlated to C29R below the K–Pg boundary on Seymour Island (930–1007 m) (Fig. 8), suggests Deccan eruptions did not perturb the seawater sulfate reservoir significantly. Assuming the volumes and flux

estimates outlined above are correct, sulfur release from Deccan eruptions would equate to 5.02×10^6 MT of S, which equates to 1.57×10^{17} mol S. This is large, but is not likely to influence the much larger oceanic reservoir, even at lower Cretaceous seawater concentrations. Assuming Deccan sulfur had an isotopic composition of 0‰, an average $\delta^{34}S$ of 18‰ for the isotopic composition of late Maastrichtian seawater, and with a seawater concentration of ~2 mM (2.9×10^{18} mol S) (see Section 6.2 below for discussion of this estimate), then mass balance yields a potential change of less than 1‰ to the $\delta^{34}S$ of seawater by Deccan eruptions alone.

An indirect forcing via CO_2 induced climate warming in the late Maastrichtian is plausible, and such a warming event is recorded globally in the last few hundred thousand years of the Maastrichtian, apparently coincident with the main phase of Deccan eruptions (e.g. Henehan et al., 2016; Barnet et al., 2017). Evidence for this event at high latitudes has also been recorded from the López de Bertodano Formation (Tobin et al., 2012; Bowman et al., 2013; Petersen et al., 2016). Climate forcing could affect the global sulfur cycle via thermal expansion of the oceans and an increase in the area available for pyrite burial, and/or by decreased oxygen solubility leading to the temporary expansion of anoxic conditions. However, there is relatively little evidence for the development of these conditions during or after the Deccan warming event, and minimal perturbation to the global carbon cycle (Voigt et al., 2012; Barnet et al., 2017). In addition, the increase in $\delta^{34}S_{CAS}$ values in our dataset occurs prior to chron C29R and the onset of Deccan main phase eruptions based on recent radiometric dates (Schoene et al., 2015; Renne et al., 2015; Barnet et al., 2017). A volumetrically small, earlier phase of Deccan volcanism may have occurred during chron C30N (Chenet et al., 2009; Keller et al., 2016), but there is little or no evidence that this caused any perturbation to global climate (e.g. Thibault, 2016).

6.1.2. $\delta^{34}S_{CAS}$ at the K–Pg boundary – links to impact, mass extinction and recovery

The $\delta^{34}S_{CAS}$ values also appear to show little change at the K–Pg boundary, but a positive peak in CAS values (+19.6‰) is reached ~10 m (50–100 kyrs) above the boundary and mass extinction interval on Seymour Island (Figs. 8 and 9). Sulfur release from the Chicxulub impact event coincident with the K–Pg boundary itself (Arenillas et al., 2004; Renne et al., 2013) therefore appears to have had a negligible effect on seawater $\delta^{34}S$. The impact site on the Yucatán Peninsula was a shallow-water, carbonate platform underlain by significant (1 to more than 3 km-thick) Cretaceous evaporite and dolomite deposits (Sigurdsson et al., 1991; Brett, 1992). Volatilization of this sulfur following shock decomposition (Prescher et al., 2011), would lead to rapid release of sulfate aerosols and other gases into the atmosphere (Pierazzo et al., 1998; Pierazzo et al., 2003; Ohno et al., 2014). CO_2 release may have been exacerbated by biomass burning and atmospheric soot injection (Bardeen et al., 2017). Most recent estimates suggest the impact released 325 ± 130 Gt of sulfur and 425 ± 160 Gt of CO_2 along with significant amounts of water vapour, although the precise amount of material involved in volatile release is problematic due to a lack of precise constraint over the volume of sulfur-bearing materials excavated by the impact (Pierazzo et al., 1998; Artemieva et al., 2017). Models suggest that following an initial 'heat pulse' (Robertson, et al., 2013), a rapid and severe cooling of surface and ocean temperatures lasting decades to hundreds of years occurred in the earliest Paleocene (Kring, 2007; Robertson et al., 2013; Brugger et al., 2017). Debate continues as to the amount of time taken for fallout of sulfur-rich material from the atmosphere (e.g. Ohno et al., 2014), but this may have led to deposition of acid rain and potentially transient ocean acidification (D'Hondt et al., 1994; Maruoka et al., 2002; Tyrrell et al., 2015).

Despite these dramatic events, which could represent important kill mechanisms during the mass extinction event, the likelihood of sulfur release from the Chicxulub impact event influencing the $\delta^{34}S$ record depends primarily on the nature of the volatilized target rocks. The isotopic composition of sulfur-bearing lithologies from the Yucatán Peninsula is fortuitously provided in the compilation of Claypool et al. (1980) and has also been estimated based on the $\delta^{34}S$ values of impact melt glasses from the K–Pg boundary in Haiti (e.g. Sigurdsson et al., 1992). These sources suggest the early–late Cretaceous evaporitic and limestone sequences underlying the crater have $\delta^{34}S$ values ranging between 13‰ and ~18‰ (Claypool, 1980), reflecting their Cretaceous seawater source (e.g. Paytan et al., 2004; Gomes and Hurtgen, 2016). Impact melt glasses show more variable values down to as low as 1.5‰, implying contribution of isotopically light sulfur from crustal rocks and/or the impactor itself (Sigurdsson et al., 1992; Chaussidon et al., 1996), but the volume of material that could be attributed to these sources is difficult to quantify on a global scale (e.g. Toon et al., 2016). Importantly, because the isotopic composition of the target rocks is close to contemporaneous Cretaceous seawater, it appears there is rather limited scope for the Chicxulub impact to directly alter global $\delta^{34}S$ values despite the rapid release into the Earth system, and significantly lower than modern seawater concentrations (see Section 6.4 below). We suggest that secondary processes, notably redox and carbon cycle changes operating in the aftermath of the impact and mass extinction event, appear to have been significantly more important in terms of affecting the global sulfur cycle.

Kajiwara and Kaiho (1992) and Kaiho et al. (1999) suggested the development of a low oxygen interval in the immediate aftermath of the marine mass extinction event, based on rapid positive excursions in $\delta^{34}S_{Sulfide}$ and $\delta^{34}S_{CAS}$ at the K–Pg boundary in sections from Japan (Kawaruppu) and Spain (Caravaca) (Fig. 9B and C). Kaiho et al. (1999) bulk rock CAS data fluctuates from values of +15‰ to +22‰ across the K–Pg boundary (Fig. 9C). These data are from a thin (80 cm) stratigraphic interval; representing a very short time interval in the latest Maastrichtian and early Danian. The $\delta^{34}S_{Sulfate}$ values also rise during the earliest Danian at Caravaca where additional trace metal proxies have confirmed this low oxygen event, but suggest it was confined to the 'impact layer' of fallout located directly at the K–Pg boundary (stratigraphic extent of 1 mm) and

therefore extremely short-lived (<500 years) (De Oca et al., 2013). Maruoka et al. (2002) described positive excursions in $\delta^{34}S$ and increased C/S ratios from two terrestrial K–Pg boundary sites in the US Western Interior which occurred over similar short timescales to the marine records. They attributed these excursions to a high input of sulfate into terrestrial wetlands, either directly from deposition of (^{34}S enriched) ejecta, or a short-lived period of acid rain deposition which caused the temporary development of anoxic conditions. Most evidence from both marine and terrestrial records therefore points towards a general positive excursion in sulfur isotope values in the immediate aftermath of the Chicxulub impact event.

Attempted comparison between Seymour Island and contemporaneous lower latitude marine sulfur isotope K–Pg datasets is shown in Fig. 9. Absolute correlation is not possible beyond the known position of the K–Pg boundary due to the lack of datum levels for direct correlation. Magnetochron reversals are also used as tie-points from Seymour Island, but both published datasets come from a short interval in chron C29R. Published age models (Kaiho and Saito, 1986; Arenillas et al., 2004) would suggest the perturbations to the sulfur cycle recorded at the K–Pg boundary are confined to the P0 (*Guembelitria cretacea*) foraminiferal biozone in both Spain and Japan, with a suggested duration of 18–21 kyrs of the early Paleocene (Arenillas et al., 2004). This is also true for the terrestrial sulfur isotope dataset of Maruoka et al. (2002). Using published age models from the López de Bertodano Formation (Tobin et al., 2012; Bowman et al., 2013; Witts et al., 2016), an equivalent interval on Seymour Island would likely bracket a 4 m-thick glauconite-rich interval immediately above the K–Pg boundary (Fig. 9), although this must also be regarded as a tentative correlation given the fact that such horizons may represent intervals of slow sedimentation or be associated with lateral facies boundaries (Bowman et al., 2016).

Additional evidence for transient anoxic conditions after the K–Pg boundary have been described from several sites, but there is limited evidence for a significant anoxic event globally (e.g. Alegret and Thomas, 2005; Schoepfer et al., 2017). A short-lived expansion of oxygen minimum zones globally following the extinction is possible, due to either a flux of organic material and mass die-off, or collapse of the biological pump (D'Hondt, 2005) and enhanced remineralization of organic matter in the photic zone (Vellekoop et al., 2017). Similarly, short-lived changes in global ocean circulation following the impact winter could also have contributed to this phenomenon, although this is not well quantified (Brugger et al., 2017). Evidence from the size distribution of pyrite framboids and trace element enrichments in bulk sediment provide evidence for fluctuating benthic redox conditions in the post-boundary interval in Antarctica (Witts et al., 2016; Schoepfer et al., 2017). This same stratigraphic interval also contains abundant articulated and disarticulated fish remains; the only such horizon on Seymour Island (Zinsmeister, 1998). This appears to indicate the temporary development of harsh conditions in the water column and on the sea floor in Antarctica during the immediate aftermath (initial 10 s kyrs) of the mass extinction, and it is therefore plausible that the final increase in $\delta^{34}S_{CAS}$ values above the K–Pg boundary on Seymour Island was driven by a global rapid increase in anoxic deposition and pyrite burial in the earliest Paleocene.

Following a ~30 m stratigraphic gap in our data due to elimination of samples considered to be diagenetically altered, a rapid negative excursion of 3–4‰ in $\delta^{34}S_{CAS}$ occurs in the early Paleocene. Values of $\delta^{34}S_{CAS}$ values then return to a pre-extinction baseline of ~17–19‰, like those of the late Maastrichtian (Fig. 8; Fig. 9A). This drop and recovery occurs entirely within a stratigraphic interval that is correlated to magnetochron C29R, and therefore ~320 kyrs following the K–Pg (Tobin et al., 2012; Bowman et al., 2013; Witts et al., 2016). In interpreting this dramatic trend it is important to note that of the various models for the nature of the post-K–Pg ocean, a significant reduction in organic carbon burial would be most likely to impact significantly on the global sulfur cycle in this way, due to the importance of organic carbon as an electron donor in the process of MSR and subsequently, pyrite formation. The negative excursion in $\delta^{34}S_{CAS}$ in the early Paleocene followed by a rapid recovery could therefore be the result of a significant decrease in pyrite burial associated with a large drop in carbon burial globally, as suggested by the collapse of the deep-sea carbon isotope gradient and weakening of the biological pump (Kump, 1991; D'Hondt, 2005; Esmeray-Senlet et al., 2015).

The lack of an immediate sulfur cycle response at the K–Pg boundary itself therefore reflects the time taken to move reactive organic carbon through the zone of early diagenesis in marine sediments, since this is the primary control on pyrite sulfur burial flux. Despite the sudden reduction of carbon flux and subsequent burial following the mass extinction (e.g. D'Hondt, 2005; Esmeray-Senlet et al., 2015), pre-boundary reactive organic carbon would still be available for pyrite formation into the earliest Danian. Only after this is exhausted would the sulfur cycle respond with an associated decrease in pyrite burial.

6.2. Sulfur cycle box model for estimating response of seawater $\delta^{34}S$ to potential perturbations during the early Paleocene

To assess the validity of this hypothesis and implications for Cretaceous–Paleocene seawater chemistry, we conducted some simple box model experiments to estimate the likely response of the sulfur cycle to changes in pyrite burial rate and other potential causal mechanisms for this negative excursion in the aftermath of the K–Pg mass extinction – specifically changes in weathering rates and the fractionation factor between seawater sulfate and coeval microbially-produced hydrogen sulfide. The long term $\delta^{34}S$ composition of ocean sulfate can be modelled using a simple box-flux representation (e.g. Garrels and Lerman, 1984; Berner, 1987). The boxes and fluxes in our model are shown in Fig. 10a and Table 3. Burial fluxes move sulfur from the ocean (S) to the sediments in either reduced (modelled as pyrite, PYR) or oxidised (modelled as gypsum, GYP) forms. Due to biological preference for

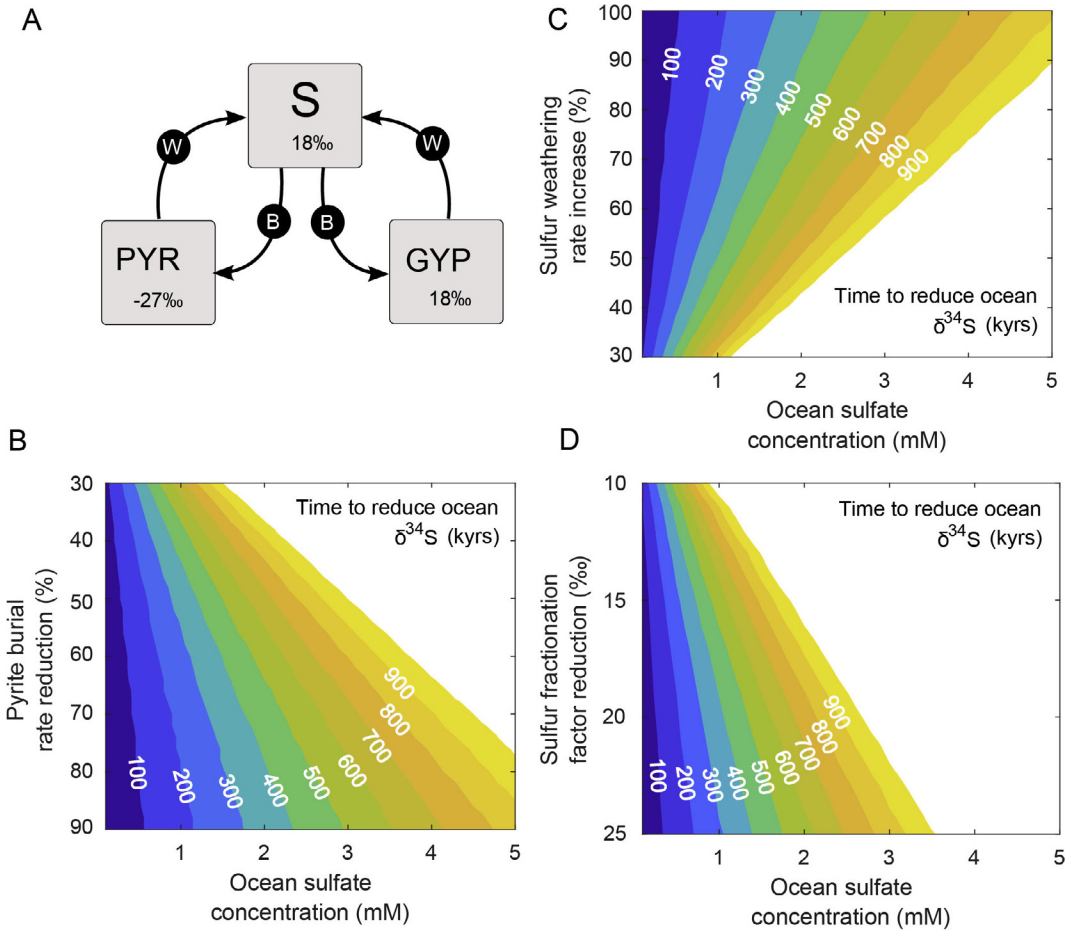

Fig. 10. Sulphur cycle box model summary. A. Boxes and fluxes: Here S represents ocean sulphate, PYR represents sedimentary pyrite, and GYP represents sedimentary gypsum. Average fractionations shown in per mil (‰ VCDT). Burial processes are labelled 'B', weathering and degassing processes are labelled 'W'. A fractionation factor of $\Delta S = 45‰$ between oceanic sulphate and sedimentary pyrite is assumed. The remaining panels show output phase spaces where the contours denote the time taken (in kyrs) for $\delta^{34}S$ of ocean sulphate to drop by 3‰, with respect to the initial ocean sulphate concentration and a given perturbation. B. Perturbation to pyrite burial (B_{PYR}), shown as a percentage reduction. C. Perturbation to total sulphur weathering input ($W_{PYR} + W_{GYP}$), shown as a percentage increase. D. Perturbation to sulphur fraction factor (ΔS), shown as a per mille reduction. All perturbations are applied permanently.

Table 3
Fluxes and parameters for sulfur cycle box model.

Flux	Symbol	Rate
Pyrite weathering	W_{PYR}	Fixed at $k_{PYR} = 0.7 \times 10^{12} mol\ yr^{-1}$
Pyrite burial	B_{PYR}	Varied in experiments
Gypsum weathering	W_{GYP}	Fixed at $k_{GYP} = 1 \times 10^{12} mol\ yr^{-1}$
Gypsum burial	B_{GYP}	$k_{GYP}\left(\frac{S}{S_{steady}}\right)$
Parameter	**Symbol**	**Value**
Ocean sulfate	S	Varied in experiments
Steady state ocean sulfate	S_{steady}	Varied in experiments
Isotopic composition of S	δ_S	Predicted from model
Isotopic composition of PYR	δ_{PYR}	Fixed at −27‰
Isotopic composition of GYP	δ_{GYP}	Fixed at 18‰
Fractionation factor: sulfur	ΔS	Fixed at 45‰

the lighter sulfur isotope during microbial sulfate reduction, buried pyrite is isotopically lighter than the seawater sulfate it is derived from. The fractionation effect is denoted ΔS, and is usually assumed to be constant at 45‰ (Canfield, 2001) (but see Brunner and Bernasconi (2005) for discussion). The isotopic composition of seawater sulfate is gov-

erned by the composition of the sedimentary reservoirs, the fractionation factor ΔS, and the relative rates of pyrite and gypsum burial and weathering. The timing of the response of seawater sulfate $\delta^{34}S$ to changes in burial and weathering fluxes depends on sulfate concentration, with lower sulfate concentrations permitting faster shifts in isotopic composition (e.g. Algeo et al., 2015).

Initially we fix the input rates of pyrite and gypsum (W_{PYR}, W_{GYP}) at present day estimates, with pyrite constituting ~40% of the total sulfur flux (Canfield, 2013). The gypsum burial flux is assumed proportional to the ocean sulfate concentration (Bergman et al., 2004). We run the model from this steady state for a range of different ocean sulfate concentrations, and impose variation in either the rate of pyrite burial, the overall weathering input, or the fractionation factor ΔS in order to observe the timescale and magnitude of changes in ocean $\delta^{34}S$. The model solves the following differential equations for the abundance and isotopic composition of seawater sulfate:

$$\frac{dS}{dt} = W_{PYR} + W_{GYP} - B_{PYR} - B_{GYP} \quad (1)$$

$$\frac{d(S \times \delta S)}{dt} = W_{PYR}\delta_{PYR} + W_{GYP}\delta_{GYP} - B_{PYR}(\delta_S - \Delta S) - B_{GYP}\delta_S \quad (2)$$

Eq. (1) represents the inputs and outputs of seawater sulfate via weathering and burial processes. Eq. (2) is an isotope mass balance for the quantity $S \times \delta S$, which considers isotopic inputs and outputs. To find the isotopic composition of seawater sulfate, we compute $\delta_S = \frac{(S \times \delta_S)}{S}$. The system of equations is solved in MATLAB using the ODE suite. Full model code is available on request.

Fig. 10b shows the time taken for ocean sulfate $\delta^{34}S$ to drop from 18‰ to 15‰ under a variety of ocean sulfate concentrations and perturbations to the pyrite burial rate. The model requires pyrite burial to be reduced by >15% to drive the observed change in sulfate $\delta^{34}S$ on any timescale. Greater reductions in pyrite burial cause more rapid responses from $\delta^{34}S$. For example, assuming $[SO_4] = 3$ mM, a 50% reduction in pyrite burial causes a 3‰ drop in ocean $\delta^{34}S$ over around 1 million years, whereas a 90% reduction in pyrite burial causes the same reduction over 500,000 years.

We also tested two alternative hypotheses to explain the negative excursion, firstly via increased weathering rates, which would bring more isotopically light sulfur into the oceans via increased riverine input (Bottrell and Newton, 2006). Changes in global weathering rates have been hypothesised in the aftermath of the K–Pg mass extinction, with reports of positive excursions in strontium (Sr) isotope values during the earliest Danian from several sites (e.g. Martin and Macdougall, 1991; Vonhof and Smit, 1997). These data were questioned by McArthur et al. (1998) who suggested these spikes simply represented diagenetic artifacts rather than increased weathering. Additional direct evidence for weathering changes is provided by an enigmatic short-lived 5‰ negative excursion in seawater lithium isotopes across the K–Pg boundary (Misra and Froelich, 2012), which was suggested to represent continental denudation and acid rain-enhanced weathering on a global scale over <0.5 myrs following the Chicxulub impact. A global increase in weathering rates causes similar isotopic shifts as a decrease in pyrite burial in our model (for example a 70% increase in total weathering input produces a similar isotopic response to a 50% reduction in pyrite burial; see Fig. 10c). However, evidence for such large changes in global weathering rates across the K–Pg boundary remain to be validated by additional records, and it is unclear whether the magnitude of change required by the model is realistic given the available geological data.

Another way to drive negative $\delta^{34}S$ excursions is to reduce the fractionation factor ΔS. This is governed by a complex array of factors, but changes to the rate of sulfate reduction - chiefly driven by the quantity and quality of organic carbon delivery and the extent of shallow marine environments where MSR occurs - and sulfate concentration, are probably the most relevant for the aftermarth of the K–Pg on a global scale (e.g. Sim et al., 2011; Leavitt et al., 2013). Fig. 10d plots the model response to decreasing ΔS below its 45‰ default, and shows that both a reduction of more than 20‰ and a very low sulphate concentration (<1 mM) are required to replicate the observed changes over 300 kyrs.

Decreased ΔS values are usually associated with increased MSR rates and increased input/availability of labile organic matter, whereas the loss of quantity and quality of organic carbon burial typically leads to decreased MSR rates, and an increase in fractionation and ΔS values (Leavitt et al., 2013). It is difficult to reconcile decreasing ΔS as an explanation for the negative excursion in $\delta^{34}S_{CAS}$ with available evidence for primary paleoceanographic conditions following the K–Pg mass extinction. As previously mentioned, the early Danian saw a general decrease in organic carbon export and bural (Hsü and McKenzie, 1985; Kump, 1991; Esmeray-Senlet et al., 2015), and while primary production itself recovered rapidly, perhaps driven by groups such as dinoflagellates or cyanobacteria (Sepúlveda et al., 2009), the massive extinctions of groups at the base of the oceanic food chain probably also changed the nature (and therefore lability) of organic carbon being exported in earliest Paleocene oceans (Alegret et al., 2012; Vellekoop et al., 2017). Such a scenario might be expected to lead to decreased rates of MSR on a global scale. In terms of changes to sulfate concentrations, whilst it is possible to calculate potential values for the latest Cretaceous and earliest Paleocene ocean based on the rate of change in our dataset (see Section 6.4 below), there is little or no data for significant changes in concentration across the K–Pg boundary which could have driven changes in ΔS. For example, bulk rock $\delta^{34}S_{CAS}$ and $\delta^{34}S_{Pyrite}$ data from Caravaca show similar ΔS values either side of the aforementioned perturbation at the boundary itself (Kaiho et al., 1999).

Although the available geological data and our modelling studies support the reduction in organic carbon burial following the K–Pg mass extinction as the primary mechanism behind the changes we see in the $\delta^{34}S_{CAS}$ record from Seymour Island, we cannot rule out a subsidiary role for contributions from an increased weathering flux based on the results of box modelling studies. It is important to point

out that a combination of these two factors could produce the observed changes in our isotope record. Changes to ΔS could also plausibly act in concert with these two drivers, but this is considered less likely given the evidence outlined above.

6.3. Implications for latest Cretaceous and early Paleocene seawater sulfate concentrations

To produce a 3‰ reduction in ocean $\delta^{34}S$ over ~300 kyrs, in line with our data (and the assumption that the signal is global), requires an ocean sulfate concentration of <2 mM, regardless of the reduction in pyrite burial rate or any reasonable modification to other parameters in our box model. The 'rate method' of Algeo et al. (2015) derives a sulfate concentration of 2–5 mM under the same timescale constraints. Our reduction in the lower limit derives from the system dynamics – ocean sulfate concentration begins to increase in the model as the pyrite burial sink is restricted (or as the weathering input is increased), causing an increase in the rate of deposition of gypsum (Fig. 11). Both

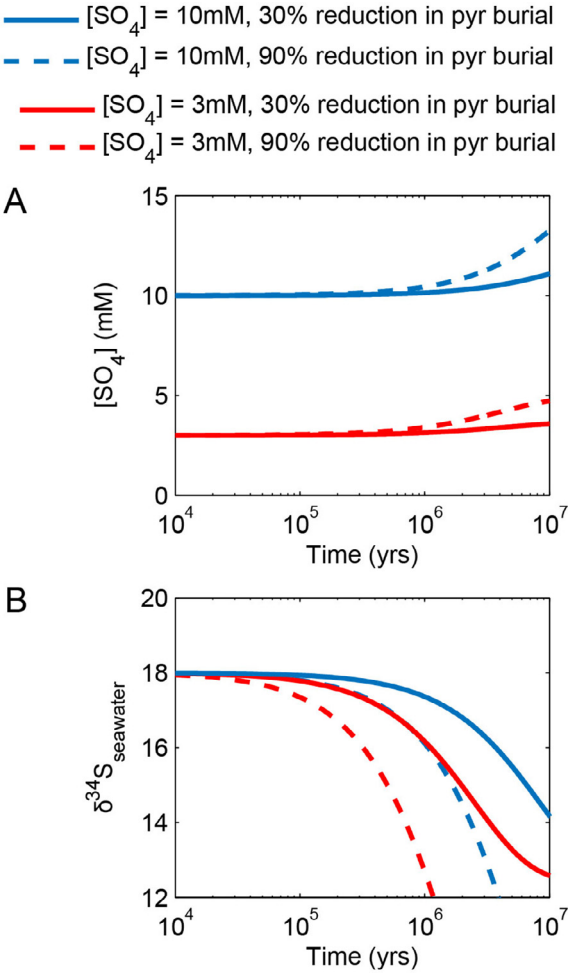

Fig. 11. Examples of time-dependent model runs, with perturbation occurring at t = 0. A. Ocean sulfate inventory. B. Ocean sulfate $\delta^{34}S$. As in Fig. 10, note that both $[SO_4]$ and the degree of change in pyrite burial impact the timeframe of the $\delta^{34}S$ response.

feedbacks tend to buffer against rapid changes in $\delta^{34}S$, and thus a lower sulfate concentration is estimated here than by the rate method. The primary implication of all modelled scenarios is therefore that early Paleocene seawater sulfate concentrations must have been an order of magnitude lower than in the modern to achieve the isotope excursion implicated by the data presented here.

Estimates of seawater sulfate concentrations from sparse fluid inclusion data suggest values ranging as low as 5 mM to as high as 23 mM for the Cretaceous to early Cenozoic time interval (Horita et al., 2002; Lowenstein et al., 2003; Timofeeff et al., 2006; Brennan et al., 2013). Modelling studies using a variety of methods indicate values for the Maastrichtian of ~5 mM (Wortmann and Paytan, 2012), ~11 mM (Berner, 2004), or ~15 mM (Demicco et al., 2005), all significantly lower than the present day. Recent work by Hall et al. (2016) found evidence for a strong, unequivocal, methane-derived DIC signal in the form of large-amplitude annual cycles of carbon isotopic variability in molluscan carbonate taken from the same Cretaceous–Paleocene stratigraphic sections on Seymour Island. These authors suggest that the increased importance of methanogenesis and methanotrophy in influencing the isotopic composition of bottom water DIC, is only possible because of lower-than-modern seawater sulphate concentrations. Our estimate of low sulfate concentration is therefore consistent with this hypothesis, but indicate that the release of substantial methane derived DIC would perhaps not become prominent until sulfate concentrations fall to the lower end of the range of estimates for the latest Cretaceous and early Paleogene (e.g. Horita et al., 2002; Brennan et al., 2013; Wortmann and Paytan, 2012).

6.4. Recovery of biogeochemical cycles and biodiversity in the early Paleocene: biosphere-geosphere links?

Based on linear interpolation of sedimentation rates and correlation with the magnetostratigraphic record of Tobin et al. (2012), the timing of the subsequent rapid rise in $\delta^{34}S_{CAS}$ to values close to pre-extinction 'background' occurs close to the base of magnetochron C29N, ~320 kyrs after the K–Pg boundary (Fig. 12). On a global scale, this time interval encompasses the initial recovery of the surface-deep water carbon isotopic gradient in the deep ocean (Stage 1–2 boundary of Birch et al. 2016 see also Coxall et al., 2006), and is also characterised by stabilising diversity in benthic foraminiferal faunas (Alegret and Thomas, 2007) and initial recovery of calcareous nannoplankton floras, which are severely affected (>90% extinction) at the K–Pg boundary (Jiang et al., 2010). Intriguingly, it also corresponds with the short-lived 'Dan-C2' hyperthermal event recorded as a series of short, but prominent negative carbon isotope excursions in deep sea and land-based sections (Coccioni et al., 2010) although any link between the two has not been established.

On Seymour Island, sulfur cycle recovery also coincides with the stratigraphic interval where species richness (alpha diversity) in benthic molluscan faunas (bivalves and gas-

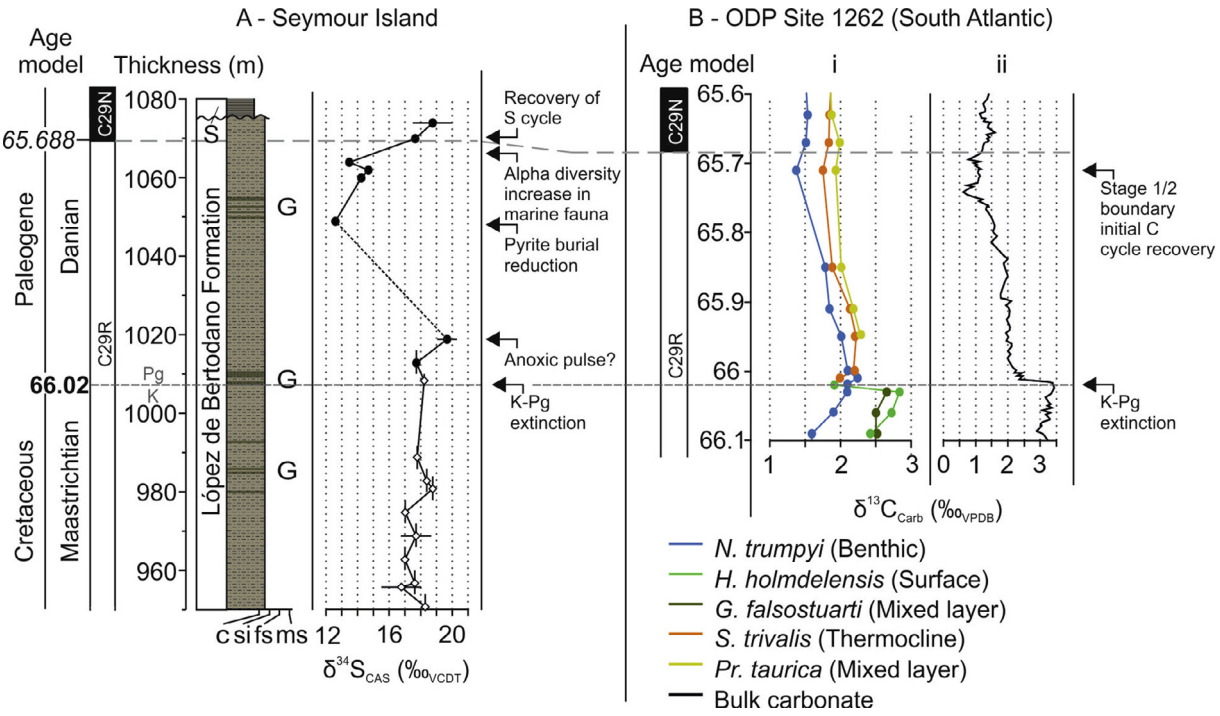

Fig. 12. Correlation of sulfur and carbon cycle records and associated events in the early Paleocene. A: $\delta^{34}S_{CAS}$ data from this study through the uppermost López de Bertodano Formation (Seymour Island) correlated to magnetostratigraphy of Tobin et al. (2012), ages of chron reversals from GTS2012 (Gradstein et al., 2012). For explanation of symbols in A see Fig. 9. B: Foraminiferal and bulk carbon isotope records from ODP Site 1262 (Walvis Ridge, central Atlantic). Age model from Dinarès-Turrell et al. (2014). i = carbon isotope data from planktonic and benthic foraminifera across the K–Pg boundary from Birch et al. (2016), showing collapse of surface-deep water carbon isotope gradient. Coloured lines represent different species of foraminifera: *N. truempyi* = *Nuttalides*, *H.holmdelensis* = *Hedbergella*, *G. falsostuarti* = *Globotruncana*, *S. trivalis* = *Subbotina*, *Pr. taurica* = *Praemurica*. ii = bulk carbon isotope data from Kroon et al. (2007) showing decrease coincident with the K–Pg boundary and mass extinction. Stage 1/2 boundary of Birch et al. (2016) marks the initial recovery of the carbon isotope gradient between surface and deep waters, (increase in export productivity) and coincides temporally with recovery of the Seymour Island $\delta^{34}S_{CAS}$ dataset to pre-extinction values. Dashed grey lines mark tentative correlation between magnetostratigraphic tie-points. (For interpretation of the references to colour in this figure legend, the reader is referred to the web version of this article.)

tropods) begins to increase following the K–Pg mass extinction, with the immigration of new species of gastropods from South America (Crame et al., 2014; Witts et al., 2016) (Fig. 12). This precedes full recovery of the marine fauna, which takes place in the overlying Danian-age Sobral Formation (Bowman et al., 2016). Taken together, these various data would suggest close links between stabilisation of carbon and sulfur cycling, and marine ecosystem recovery following the K–Pg extinction event. This provides some support for general models of post-extinction ecosystems which closely link processes in both the biosphere and geosphere (e.g. Hull, 2015).

To summarise, the data presented herein suggests a reduction in export productivity and decrease in organic carbon burial, perhaps accompanied by an increased weathering flux over several 100 kyrs following the K–Pg boundary, leading to a concomitant decline in global pyrite burial and decrease in ocean sulfate $\delta^{34}S$ as light weathered sulfate continues to be added to the system. About 320 kyrs after the mass extinction, the biological system starts to recover on a global scale, and carbon export to the deep ocean increased. Global pyrite burial flux therefore increases in concert with the restoration of the organic carbon flux to the sea-floor, and re-exerts its influence on the isotopic composition of seawater sulfate, driving it back towards pre-extinction values.

7. CONCLUSIONS

- We present the highest resolution seawater sulfate record ever generated for this time interval, for the first time revealing changes to the global sulfur cycle before, and after the K–Pg mass extinction event.
- Detailed assessment of sample preservation and fidelity of the record suggest factors affecting preservation of primary seawater CAS isotopes are complex and not necessarily linked to the preservation of original carbonate mineralogy or chemistry. A greater examination of the influence of local pore water chemistry and biogeochemical processes in driving changes to sulfur cycle proxies such as CAS should be considered before any primary record is interpreted.
- This study provides clear evidence of the influence of pyrite oxidation on CAS isotope compositions, and emphasises the importance of $\delta^{18}O_{CAS}$ as a tool for

assessing the influence of this process. Evidence from trace elements and carbonate carbon and oxygen isotopes indicate this process is decoupled from the normal indicators of carbonate preservation.

- Interpretation of the primary record and comparison with contemporaneous environmental changes reveals evidence for a relatively stable sulfur cycle in the early to mid-Maastrichtian (69 Ma).
- A +4‰ shift in $\delta^{34}S_{CAS}$ suggests an enigmatic late Maastrichtian increase in pyrite burial, possibly decoupled from global carbon cycle changes in the late Maastrichtian-earliest Danian by low ocean sulfate concentrations. This record may be partly influenced by short term ocean anoxia immediately following the K–Pg boundary.
- There is no evidence of the direct influence of Deccan volcanism on the seawater sulfate isotopic record during the late Maastrichtian, nor for direct influence by the Chicxulub impact. This is probably due to the buffering effect of a large seawater reservoir, and because carbonate-rich target rocks for the impact were not sufficiently isotopically distinct from contemporaneous seawater.
- Changes to the carbon cycle linked to the K–Pg mass extinction event also affected the global sulfur cycle. This is recorded in a prominent negative excursion in sulfate-S isotopes during the earliest Paleogene (66–65.7 Ma). Based on geological evidence for early Paleocene oceanographic conditions, this excursion was likely driven by the collapose in export productivity, a drop in organic carbon burial and an associated decrease in pyrite burial on a global scale. Box modelling supports this hypothesis, but suggests that an increase in the weathering flux following the K–Pg boundary may have also contributed to the development of this excursion.
- Box modelling results further suggest that to produce a 3‰ reduction in ocean $\delta^{34}S$ over ~300kyrs, in line with our early Paleocene data and regardless of driving mechanism, requires an ocean sulfate concentration of <2 mM, supporting the hypothesis that Cretaceous and early Paleogene seawater sulfate concentrations were significantly lower than the modern.

ACKNOWLEDGEMENTS

We thank the support staff and students of the Cohen Laboratories (University of Leeds), the Godwin Laboratory (University of Cambridge), National Oceanographic Centre, Southampton, and the School of Geosciences (University of Edinburgh) for technical and analytical assistance. At the University of Leeds, Lesley Neve is gratefully acknowledged for assistance with XRD analyses, and Richard Walshaw for assistance with SEM imaging and analysis. The paper benefited from the helpful reviews and comments of Benjamin Gill (Virginia Tech) and the handling editor Christian Koeberl (University of Vienna). Funding for this study was provided by a PhD scholarship from the University of Leeds – United Kingdom to James Witts, and United Kingdom Natural Environment Research Council (NERC) grants NE/C506399/1 (Antarctic Funding Initiative), NE/I00582X/1 (PALEOPOLAR) and NE/N018559/1. Fieldwork to Seymour Island was supported logistically by the British Antarctic Survey.

APPENDIX A. SUPPLEMENTARY MATERIAL

Supplementary data associated with this article can be found, in the online version, at https://doi.org/10.1016/j.gca.2018.02.037.

REFERENCES

Adams D. D., Hurtgen M. T. and Sageman B. B. (2010) Volcanic triggering of a biogeochemical cascade during Oceanic Anoxic Event 2. *Nat. Geosci.* **3**, 201–204.

Alegret L. and Thomas E. (2005) Cretaceous/Paleogene boundary bathyal palaeoenvironments in the central North Pacific (DSDP Site 465), the Northwestern Atlantic (ODP Site 1049), the Gulf of Mexico and the Tethys: the benthic foraminiferal record. *Palaeogeogr. Palaeoclimatol. Palaeoecol.* **224**, 53–82.

Alegret L. and Thomas E. (2007) Deep-sea environments across the Cretaceous/Paleogene boundary in the eastern South Atlantic Ocean (ODP Leg 208, Walvis Ridge). *Mar. Micropaleontol.* **64**, 1–17.

Alegret L., Thomas E. and Lohmann K. C. (2012) End-Cretaceous marine mass extinction not caused by productivity collapse. *Proc. Nat. Acad. Sci.* **109**, 728–732.

Algeo T. J., Luo G. M., Song H. Y., Lyons T. W. and Canfield D. E. (2015) Reconstruction of secular variation in seawater sulfate concentrations. *Biogeosciences* **12**, 2131–2151.

Alvarez L. W., Alvarez W., Asaro F. and Michel H. V. (1980) Extraterrestrial cause for the Cretaceous-Tertiary Extinction. *Science* **208**, 1095–1108.

Archibald J. D., Clemens W. A., Padian K., Rowe T., MacLeod N., Barrett P. M., Gale A., Holroyd P., Sues H.-D., Arens N. C., Horner J. R., Wilson G. P., Goodwin M. B., Brochu C. A., Lofgren D. L., Hurlbert S. H., Hartman J. H., Eberth D. A., Wignall P. B., Currie P. J., Weil A., Prasad G. V. R., Dingus L., Courtillot V., Milner A., Milner A., Bajpai S., Ward D. J. and Sahni A. (2010) Cretaceous extinctions: multiple causes. *Science* **328**, 973.

Arenillas I., Arz J. and Molina E. (2004) A new high resolution planktic foraminiferal zonation and subzonation for the lower Danian. *Lethaia* **37**, 79–95.

Artemieva N., Morgan J. and Expedition 364 Science Party (2017) Quantifying the release of Climate-Active Gases by Large Meteorite Impacts With a Case Study of Chicxulub. *Geophys. Res. Lett.* **44**, 10180–10188.

Askin R. A. and Jacobson S. R. (1988) Total Organic Carbon content and Rock Eval pyrolysis on outcrop samples across the Cretaceous/Tertiary boundary, Seymour Island, Antarctica. *Antarct. J. United States* **1988**, 37–39.

Bambach R. K. (2006) Phanerozoic biodiversity mass extinctions. *Ann. Rev. Earth Planet. Sci.* **34**, 127–155.

Bardeen C. G., Garcia R. R., Toon O. B. and Conley A. J. (2017) On transient climate change at the Cretaceous-Paleogene boundary due to atmospheric soot injections. *Proc. Nat. Acad. Sci.* **114**, E7415–E7424.

Barnet J. S. K., Littler K., Kroon D., Leng M. J., Westerhold T., Röhl U. and Zachos J. C. (2017) A new high-resolution chronology for the late Maastrichtian warming event: establishing robust temporal links with the onset of Deccan volcanism. *Geology*. https://doi.org/10.1130/G39771.1.

Barrera E. and Savin S. M. (1999) Evolution of late Campanian–Maastrichtian marine climates and oceans. In: Barrera E., Johnson C. C. (Eds.), Evolution of the Cretaceous Ocean-Climate System. Geological Society of America Special Paper 332, pp. 245–282.

Bergman N. M., Lenton T. M. and Watson A. J. (2004) COPSE: a new model of biogeochemical cycling over Phanerozoic time. *Am. J. Sci.* **304**, 397–437.

Berner R. A. (1982) Burial of organic carbon and pyrite sulfur in the modern ocean: its geochemical and environmental significance. *Am. J. Sci.* **282**, 451–473.

Berner R. A. (1987) Models for carbon and sulfur cycles, and atmospheric oxygen: application to Paleozoic geologic history. *Am. J. Sci.* **287**, 177–196.

Berner R. A. and Canfield D. E. (1989) A new model for atmospheric oxygen over Phanerozoic time. *Am. J. Sci.* **298**, 333–361.

Berner R. A. (2004) A model for calcium, magnesium, and sulfate in seawater over Phanerozoic time. *Am. J. Sci.* **304**, 438–453.

Birch H. S., Coxall H. K., Pearson P. N., Kroon D. and Schmidt D. N. (2016) Partial collapse of the marine carbon pump after the Cretaceous-Paleogene boundary. *Geology* **44**, 287–290.

Bottrell S. H. and Newton R. J. (2006) Reconstruction of changes in global sulfur cycling from marine sulfate isotopes. *Earth Sci. Rev.* **75**, 59–83.

Bowman V. C., Francis J. E. and Riding J. B. (2013) Late Cretaceous winter sea ice in Antarctica? *Geology* **41**, 1227–1230.

Bowman V. C., Ineson J., Riding J., Crame J., Francis J., Condon D., Whittle R. and Ferraccioli F. (2016) The Paleocene of Antarctica: Dinoflagellate cyst biostratigraphy, chronostratigraphy and implications for the palaeo-Pacific margin of Gondwana. *Gond. Res.*. https://doi.org/10.1016/j.gr.2015.10.018.

Bowman V. C., Francis J. E., Askin R. A., Riding J. B. and Swindles G. T. (2014) Latest Cretaceous–earliest Paleogene vegetation and climate change at the high southern latitudes: palynological evidence from Seymour Island, Antarctic Peninsula. *Palaeogeogr. Palaeoclimatol. Palaeoecol.* **408**, 26–47.

Bowman V. C., Francis J. E., Riding J. B., Hunter S. J. and Haywood A. M. (2012) A latest Cretaceous to earliest Paleogene dinoflagellate cyst zonation from Antarctica, and implications for phytoprovincialism in the high southern latitudes. *Rev. Palaeobot. Palynol.* **171**, 40–56.

Brand U. and Veizer J. (1980) Chemical diagenesis of a multicomponent carbonate system - 1: Trace elements. *J. Sediment. Res.* **50**, 1219–1236.

Brennan S. T., Lowenstein T. K. and Cendón D. I. (2013) The Major-Ion composition of Cenozoic seawater: The past 36 million years from fluid inclusions in marine halite. *Am. J. Sci.* **313**, 713–775.

Brett R. (1992) The Cretaceous-Tertiary extinction: a lethal mechanism involving anhydrite target rocks. *Geochim. Cosmochim. Acta* **56**, 3603–3606.

Brugger J., Feulner G. and Petri S. (2017) Baby, it's cold outside: Climate model simulations of the effects of the asteroid impact at the end of the Cretaceous. *Geophys. Res. Lett.* **44**, 419–427.

Brunner B. and Bernasconi S. M. (2005) A revised isotope fractionation model for dissimilatory sulfate reduction in sulfate reducing bacteria. *Geochim. Cosmochim. Acta* **69**, 4759–4771.

Busenberg E. and Plummer L. N. (1985) Kinetic and thermodynamic factors controlling the distribution of SO_4 an Na+ in calcites and selected aragonites. *Geochem. Cosmochem. Acta* **49**, 713–725.

Callegaro S., Baker D. R., de Min A., Marzoli A., Geraki K., Bertrand H., Viti C. and Nestola F. (2014) Microanalyses link sulfur from large igneous provinces and Mesozoic mass extinctions. *Geology* **42**, 895–898.

Canfield D. E. (2001) Isotope fractionation by natural populations of sulfate-reducing bacteria. *Geochem. Cosmochim. Acta* **65**, 1117–11124.

Canfield D. E. (2013) Sulfur isotopes in coal constrain the evolution of the Phanerozoic sulfur cycle. *Proc. Nat. Acad. Sci. USA* **110**, 8443–8446. https://doi.org/10.1073/pnas.1306450110.

Canfield D. E., Farquhar J. and Zerkle A. L. (2010) High isotope fractionations during sulfate reduction in a low-sulfate euxinic ocean analog. *Geology* **38**, 415–418.

Chaussidon M., Sigurdsson H. and Métrich N. (1996) Sulfur and boron isotope study of high-Ca impact glasses from the K/T boundary: Constraints on source rocks. In: Ryder G., Fastovsky D. and Gartner S. (Eds.), The Cretaceous-Tertiary Event and Other Catastrophes in Earth History. Geological Society of America Special Paper, vol. 307, pp. 254–262.

Chenet A.-L., Courtillot V., Fluteau F., Gérard M., Quidelleur X., Khadri S. F. R., Subbarao K. V. and Thordarson T. (2009) Determination of rapid Deccan eruptions across the Cretaceous-Tertiary boundary using paleomagnetic secular variation: 2. Constraints from analysis of eight new sections and synthesis for a 3500-m-thick composite section. *J. Geophys. Res.* **114**, B06103. https://doi.org/10.1029/2008JB005644.

Claypool G. E., Holser W. T., Kaplan I. R., Sakai H. and Zak I. (1980) The age curves of sulfur and oxygen isotopes in marine sulfate and their mutual interpretation. *Chem. Geol.* **28**, 199–260.

Coccioni R., Frontalini F., Bancalá G., Fornaciari E., Jovane L. and Sprovieri M. (2010) The Dan-C2 hyperthermal event at Gubbio (Italy): global implications, environmental effects, and cause(s). *Earth Planet. Sci. Lett.* **297**, 298–305.

Courtillot V. and Fluteau F. (2010) Cretaceous extinctions: the volcanic hypothesis. *Science* **328**, 973–974.

Coxall H. K., D'Hondt S. and Zachos J. C. (2006) Pelagic evolution and environmental recovery after the Cretaceous-Paleogene mass extinction. *Geology* **34**, 297–300.

Crame J. A., Lomas S. A., Pirrie D. and Luther A. (1996) Late Cretaceous extinction patterns in Antarctica. *J. Geol. Soc. London* **153**, 503–506.

Crame J. A., McArthur J. M., Pirrie D. and Riding J. B. (1999) Strontium isotope correlation of the basal Maastrichtian Stage in Antarctica to the European and US biostratigraphic schemes. *J. Geol. Soc. London* **156**, 957–964.

Crame J. A., Francis J. E., Cantrill D. E. and Pirrie D. (2004) Maastrichtian stratigraphy of Antarctica. *Cretac. Res.* **25**, 411–423.

Crame J. A., Beu A. G., Ineson J. R., Francis J. E., Whittle R. J. and Bowman V. C. (2014) The early origins of the Antarctic marine fauna and its evolutionary implications. *PLoS ONE* **9**, e114732.

Cramer B. S., Toggweiler J. R., Wright J. D., Katz M. E. and Miller K. G. (2009) Ocean overturning since the late cretaceous: Inferences from a new benthic foraminiferal isotope compilation. *Paleoceanography* **24**.

D'Hondt S., Pilson M. E. Q., Sigurdsson H., Hanson, Jr, A. K. and Carey S. (1994) Surface-water acidification and extinction at the Cretaceous-Tertiary boundary. *Geology* **22**, 983–986.

D'Hondt S. (2005) Consequences of the Cretaceous/Paleogene mass extinction for marine ecosystems. *Ann. Rev. Ecol., Evol., System.* **36**, 295–317.

Demicco R. V., Lowenstein T. K., Hardie L. A. and Spencer R. J. (2005) Model of seawater composition for the Phanerozoic. *Geology* **33**, 877–880.

De Oca C. S. M., Martínez-Ruiz F. and Rodríguez-Tovar F. J. (2013) Bottom-water conditions in a marine basin after the Cretaceous-Paleogene impact event: timing the recovery of oxygen levels and productivity. *PLOS One*. https://doi.org/10.1371/journal.pone.0082242.

Dinarès-Turrell J., Westerhold T., Pujalte V., Röhl U. and Kroon D. (2014) Astronomical calibration of the Danian stage (Early Paleocene) revisited: settling chronologies of sedimentary records across the Atlantic and Pacific Oceans. *Earth Planet. Sci. Lett.* **405**, 119–131.

Ditchfield P. W., Marshall J. D. and Pirrie D. (1994) High latitude Palaeotemperature variation: new data from the Tithonian to Eocene of James Ross Island, Antarctica. *Palaeogeogr. Palaeoclimatol. Palaeoecol.* **107**, 79–101.

Dubicka Z. and Peryt D. (2012) Latest Campanian and Maastrichtian palaeoenvironmental changes: implications from an epicontinental sea (SE Poland and western Ukraine). *Cretac. Res.* **37**, 272–284.

Elliot D. H. (1988) Tectonic setting and evolution of the James Ross Basin, northern Antarctic Peninsula. In: Feldmann R. M., Woodburne M. O. (Eds.), Geology and Paleontology of Seymour Island, Antarctic Peninsula. Geological Society of America, Memoirs, vol. 169, pp. 541–555.

Elliot D. H., Askin R. A., Kyte F. T. and Zinsmeister W. J. (1994) Iridium and dinocysts at the Cretaceous-Tertiary boundary on Seymour Island, Antarctica: implication for the K-T event. *Geology* **22**, 675–678.

Esmeray-Senlet S., Wright J. D., Olsson R. K., Miller K. G., Browning J. V. and Quan T. M. (2015) Evidence for reduced export productivity following the Cretaceous/Paleogene mass extinction. *Paleoceanography* **30**, 718–738.

Feldmann R. M. and Woodburne M. O. (Eds.) (1988) Geology and Paleontology of Seymour Island, Antarctic Peninsula 169. Memoir, Geological Society of America.

Fichtner V., Strauss H., Immenhauser A., Buhl D., Neuser R. D. and Niedermayr A. (2017) Diagenesis of carbonate associated sulfate. *Chem. Geol.* **463**, 61–75.

Fike D. A., Bradley A. S. and Rose C. V. (2015) Rethinking the ancient sulfur cycle. *Ann. Rev. Earth Planet. Sci.* **43**, 593–622.

Friedrich O., Norris R. D. and Erbacher J. (2012) Evolution of middle to Late Cretaceous oceans—a 55 m.y. record of Earth's temperature and carbon cycle. *Geology* **40**, 107–110.

Garrels R. M. and Lerman A. (1984) Coupling of the sedimentary sulfur and carbon cycles - an improved model. *Am. J. Sci.* **284**, 989–1007.

Gill B. C., Lyons T. W. and Frank T. D. (2008) Behavior of carbonate-associated sulfate during meteoric diagenesis and implications for the sulfur isotope paleoproxy. *Geochim. Cosmochim. Acta* **72**, 4699–4711.

Gill B. C., Lyons T. W. and Jenkyns H. C. (2011) A global perturbation to the sulfur cycle during the Toarcian Oceanic Anoxic Event. *Earth Planet. Sci. Lett.* **312**, 484–496.

Gomes M. L., Hurtgen M. T. and Sageman B. B. (2016) Biogeochemical sulfur cycling during Cretaceous oceanic anoxic events: a comparison of OAE1a and OAE2. *Paleoceanography* **31**, 233–251.

Gradstein F. M., Ogg J. G., Schmitz M. and Ogg G. (2012) *The Geological Time Scale*. Elsevier Science Ltd, Boston.

Hall J. L. O., Newton R. J., Witts J. D., Francis J. E., Harper E. M., Crame J. A. and Haywood A. M. (2016) Extreme methane signals in a low sulfate world. *Goldschmidt Abstracts*, 1031.

Haq B. U. (2014) Cretaceous eustasy revisited. *Global Planet. Change* **113**, 44–58.

Hathway B. (2000) Continental rift to back-arc basin: Jurassic-Cretaceous stratigraphical and structural evolution of the Larsen Basin, Antarctic Peninsula. *J. Geol. Soc. London* **157**, 417–432.

Henehan M. J., Hull P. M., Penman D. E., Rae J. W. B. and Schmidt D. N. (2016) Biogeochemical significance of pelagic ecosystem function: an end-cretaceous case study. *Philos. Trans. R. Soc. B: Biol. Sci.* **371**, 20150510.

Holt N. M., Garcia-Veiga J., Lowenstein T. K., Giles P. S. and Williams-Stroud S. (2014) The major ion composition of Carboniferous seawater. *Geochim. Cosmochim. Acta* **134**, 317–334.

Horita J., Zimmermann H. and Holland H. D. (2002) Chemical evolution of seawater during the Phanerozoic: implications from the record of marine evaporites. *Geochim. Cosmochim Acta* **66**, 3733–3756.

Hsü K. J. and McKenzie J. A. (1985) A "Strangelove" ocean in the earliest Tertiary. In: Sunquist E. T. and Broecker W. S. (Eds.), The Carbon Cycle and Atmospheric CO2: Natural Variations Archaean to Present. American Geophysical Union, Washington D.C., pp. 487–492.

Hull P. (2015) Life in the Aftermath of Mass Extinctions. *Curr. Biol.* **25**, R941–R952.

Jiang S., Bralower T. J., Patzkowsky M. E., Kump L. R. and Schueth J. D. (2010) Geographic controls on nannoplankton extinction across the Cretaceous/Paleogene boundary. *Nat. Geosci.* **3**, 280–285.

John E. H., Wignall P. B., Newton R. J. and Bottrell S. H. (2010) $\delta^{34}S_{CAS}$ and $\delta^{18}O_{CAS}$ records during the Frasnian-Fammenian (Late Devonian) transition and their bearing on mass extinction models. *Chem. Geol.* **275**, 221–234.

Jones D. S. and Fike D. A. (2013) Dynamic sulfur and carbon cycling through the end-Ordovician extinction revealed by paired sulfate-pyrite $\delta^{34}S$. *Earth Planet. Sci. Lett.* **363**, 144–155.

Jørgensen B. B. (1982) Mineralization of organic matter in the sea bed – the role of sulfate reduction. *Nature* **296**, 643–645.

Jørgensen B. B. and Kasten S. (2006) Sulfur cycling and methane oxidation. In *Marine Geochemistry* (eds. H. D. Schulz and M. Zabel). Springer, Berlin, Heidelberg, pp. 271–309.

Jung C., Voigt S., Friedrich O., Koch M. C. and Frank M. (2013) Campanian-Maastrichtian ocean circulation in the tropical Pacific. *Paleoceanography* **28**, 562–573. https://doi.org/10.1002/palo.20051.

Kaiho K. and Saito T. (1986) Terminal Cretaceous sedimentary sequence recognized in the northernmost Japan based on planktic foraminiferal evidence. *Proc. Japan. Acad. Sci. Ser. B* **62**, 145–148.

Kaiho K., Kajiwara Y., Tazaki K., Ueshima M., Takeda N., Kawahata H., Arinobu T., Ishiwatari R., Hirai A. and Lamolda M. (1999) Oceanic primary productivity and dissolved oxygen levels at the Cretaceous/Tertiary boundary: their decrease, subsequent warming, and recovery. *Paleoceanography* **14**, 511–524.

Kajiwara Y. and Kaiho K. (1992) Oceanic anoxia at the Cretaceous/Tertiary boundary supported by the sulfur isotopic record. *Palaeogeogr. Palaeoclimatol. Palaeoecol.* **99**, 151–162.

Kampschulte A. and Strauss H. (2004) The sulfur isotopic evolution of Phanerozoic seawater based on the analysis of structurally substituted sulfate in carbonates. *Chem. Geol.* **204**, 255–286.

Kampschulte A., Bruckschen P. and Strauss H. (2001) The sulfur isotopic composition of trace sulfates in Carboniferous brachiopods: implications for coeval seawater, correlation, with other geochemical cycles and isotope stratigraphy. *Chem. Geol.* **175**, 149–173.

Keller G., Adatte T., Pardo A., Bajpai S., Khosla A. and Samant B. (2010) Cretaceous extinctions: evidence overlooked. *Science* **328**, 974–975.

Keller G., Punekar J. and Mateo P. (2016) Upheavals during the Late Maastrichtian: volcanism, climate and faunal events preceding the end-Cretaceous mass extinction. *Palaeogeogr. Palaeoclimatol. Palaeoecol.* **441**, 137–151.

Kominz M. A., Browning J. V., Miller K. G., Sugarman P. J., Misintseva S. and Scotese C. R. (2008) Late Cretaceous to Miocene sea-level estimates from the New Jersey and Delaware coastal plain coreholes: an error analysis. *Basin Res.* **20**, 211–226.

Kring D. A. (2007) The Chicxulub impact event and its environmental consequences at the Cretaceous-Tertiary boundary. *Palaeogeogr. Palaeoclimatol. Palaeoecol.* **255**, 4–21.

Kroon D., Zachos J. C., and the Leg 208 Scientific Party (2007) Leg 208 synthesis: Cenozoic climate cycles and excursions. In: Proceedings of the Ocean Drilling Program on Scientific Results, vol. 208, 55 pp.

Kump L. R. (1991) Interpreting carbon-isotope excursions: Strangelove oceans. *Geology* **19**, 299–302.

Kurihara K., Kano M., Sawamura H. and Sato Y. (2016) The last surviving ammonoid at the end of the Cretaceous in the north Pacific region. *Paleontol. Res.* **20**, 116–120.

Kurtz A. C., Kump L. R., Arthur M. A., Zachos J. C. and Paytan A. (2003) Early Cenozoic decoupling of the global carbon and sulfur cycles. *Paleoceanography* **18**, 1090. https://doi.org/10.1029/2003PA000908 (4).

Lawver L. A., Gahagan L. M. and Coffin M. F. (1992) The development of paleoseaways around Antarctica. In: Kennett J. P. and Warnke D. A. (Eds.), Antarctic Research Series, vol. 56, pp. 7–30.

Leavitt W. D., Halevy I., Bradley A. S. and Johnston D. T. (2013) Influence of sulfate reduction rates on the Phanerozoic sulfur isotope record. *Proc. Natl. Acad. Sci.* **110**, 11244–11249.

Li L. and Keller G. (1998) Abrupt deep-sea warming at the end of the Cretaceous. *Geology* **26**, 995–998.

Lloyd R. M. (1967) Oxygen-18 composition of oceanic sulphate. *Science* **156**, 1228–1231.

Lowenstein T. K., Hardie L. A., Timofeeff M. N. and Demicco R. V. (2003) Secular variation in seawater chemistry and the origin of calcium chloride basinal brines. *Geology* **31**, 857–860.

Lyons T. W., Walter L. M., Gellatly A.,M., Martin A. M. and Blake R. E. (2004). Sites of anomalous organic remineralization in the carbonate sediments of South Florida, USA: the sulfur cycle and carbonate associated sulfate. In: Amend J. P., Edwards K. J., and Lyons T. W. (Eds.), Sulfur Biogeochemistry—Past and Present, Geological Society of America Special Papers, vol. 379, pp. 161–176.

Macellari C. E. (1988). Stratigraphy, sedimentology and paleoecology of Upper Cretaceous/Paleocene shelf-deltaic sediments of Seymour Island (Antarctic Peninsula). In: Feldmann R. M. and Woodburne M. O. (Eds.), Geology and Paleontology of Seymour Island, Antarctic Peninsula, Geological Society of America, Memoirs, vol. 169, pp. 25–53.

MacLeod K. G., Huber B. T. and Ward P. D. (1996). The biostratigraphy and paleobiogeography of Maastrichtian inoceramids. In: Ryder G., Fastovsky D., and Gartner S. (Eds.), The Cretaceous-Tertiary Event and Other Catastrophes in Earth History, Geological Society of America Special Paper, vol. 307, pp. 361–373.

Marenco P. J., Corsetti F. A., Hammond D. E., Kaufman A. J. and Bottjer D. J. (2008a) Oxidation of pyrite during extraction of carbonate associated sulfate. *Chem. Geol.* **247**, 124–132.

Marenco P. J., Corsetti F. A., Kaufman A. J. and Bottjer D. J. (2008b) Environmental and diagenetic variations in carbonate associated sulfate: an investigation of CAS in the Lower Triassic of the western USA. *Geochim. Cosmochim. Acta* **72**, 1570–1582.

Martin E. E. and Macdougall J. D. (1991) Seawater Sr isotopes at the Cretaceous/Tertiary boundary. *Earth Planet. Sci. Lett.* **104**, 166–180.

Maruoka T., Koeberl C., Newton J., Gilmour I. and Bohor B. F. (2002) Sulfur isotopic compositions across terrestrial Cretaceous–Tertiary boundary successions. In: Koeberl C. and MacLeod K. G. (Eds.), Catastrophic Events and Mass Extinctions: Impacts and Beyond, Geological Society of America Special Paper, vol. 356, pp. 337–344.

Mazumdar A., Goldberg T. and Strauss H. (2008) Abiotic oxidation of pyrite by Fe(III) in acidic media and its implications for sulfur isotope measurements of lattice-bound sulfate in sediments. *Chem. Geol.* **253**, 30–37.

McArthur J. M., Thirlwall M. F., Engkilde M., Zinsmeister W. J. and Howarth R. J. (1998) Strontium isotope profiles across K/T boundary sequences in Denmark and Antarctica. *Earth Planet. Sci. Lett.* **160**, 179–192.

McArthur J. M., Crame J. A. and Thirlwall M. F. (2000) Definition of Late Cretaceous stage boundaries in Antarctica using strontium isotope stratigraphy. *J. Geol.* **108**, 623–640.

Miller K. G., Kominz M. A., Browning J. V., Wright J. D., Mountain G. S., Katz M. E., Sugarman P. J., Cramer B. S., Christie-Blick N. and Pekar S. F. (2005) The Phanerozoic record of global sea-level change. *Science* **310**, 1293–1298.

Misra S. and Froelich P. N. (2012) Lithium isotope history of Cenozoic seawater: changes in silicate weathering and reverse weathering. *Science* **335**, 818–823.

Molina E., Alegret L., Arenillas I., Arz J. A., Gallala N., Grajales-Nishimura, Murillo-Muneton G. and Zaghbib-Turki D. (2009) The Global Boundary Stratotype Section and Point for the base of the Danian Stage (Paleocene, Paleogene, "Tertiary", Cenozoic), auxiliary sections and correlation. Episodes 32, 84–95.

Molina E., Alegret L., Arenillas I., Arz J. A., Gallala N., Hardenbol J., von Salis K., Steurbaut E., Vandenberghe N. and Zaghbib-Turki D. (2006) The global boundary stratotype section and point for the base of the Danian stage (Paleocene, Paleogene, "Tertiary", Cenozoic) at El Kef, Tunisia – original definition and revision. *Episodes* **29**, 263–273.

Newton R. J., Pevitt E. L., Wignall P. B. and Bottrell S. H. (2004) Large shifts in the isotopic composition of seawater sulfate across the Permo-Triassic boundary in northern Italy. *Earth Planet. Sci. Lett.* **218**, 331–345.

Newton R. J., Reeves E. P., Kafousia N., Wignall P. B., Bottrell S. H. and Sha J. G. (2011) Low marine sulfate concentrations and the isolation of the European epicontinental sea during the Early Jurassic. *Geology* **39**, 7–10.

Ohno S., Kadono T., Kurosawa K., Hamura T., Sakaiya T., Shigemori K., Hironaka Y., Sano T., Watari T., Otani K. and Matsui T. (2014) Production of sulfate-rich vapour during the Chicxulub impact and implications for ocean acidification. *Nat. Geosci.* **7**, 279–282.

Olivero E. B. (2012) Sedimentary cycles, ammonite diversity and palaeoenvironmental changes in the Upper Cretaceous Marambio Group, Antarctica. *Cretac. Res.* **34**, 348–366.

Olivero E. B., Ponce J. J. and Martinioni D. R. (2008) Sedimentology and architecture of sharp based tidal sandstones in the Upper Marambio Group, Maastrichtian of Antarctica. *Sed. Geol.* **210**, 11–26.

Owens J. D., Gill B. C., Jenkyns H. C., Bates S. M., Severmann S., Kuypers M. M. M., Woodfine R. G. and Lyons T. W. (2013) Sulfur isotopes track the global extent and dynamics of euxinia during Cretaceous Oceanic Anoxic Event 2. *Proc. Nat. Acad. Sci.* **110**, 18407–18412.

Panchuk K. L., Holmden C. E. and Leslie S. A. (2006) Local controls on carbon cycling in the Ordovician midcontinent

regions of North America, with implications for carbon isotope secular curves. *J. Sediment. Res.* **76**, 200–211.

Paytan A., Kastner M., Campbell D. and Thiemens M. H. (1998) Sulfur isotopic composition of Cenozoic seawater sulfate. *Science* **282**, 1459–1462.

Paytan A., Kastner M., Campbell D. and Thiemens M. H. (2004) Seawater sulfur isotope fluctuations in the Cretaceous. *Science* **304**, 1663–1665.

Petersen S. V., Dutton A. and Lohmann K. C. (2016) End-Cretaceous extinction in Antarctica linked to both Deccan volcanism and meteorite impact via climate change. *Nat. Commun.* **7**. https://doi.org/10.1038/ncomms12079.

Pierazzo E., Kring D. A. and Melosh H. J. (1998) Hydrocode simulation of the Chicxulub impact event and the production of climatically active gases. *J. Geophys. Res.* **103**, 28607–28625.

Pierazzo E., Hahmann A. N. and Sloan L. C. (2003) Chicxulub and climate: radiative perturbations of impact-produced S-bearing gases. *Astrobiology* **3**, 99–118.

Pirrie D. and Marshall J. D. (1990) High-paleolatitude Late Cretaceous palaeotemperatures: new data from James Ross Island, Antarctica. *Geology* **18**, 31–34.

Poulton S. W., Henkel S., März C., Urquhart H., Flögel S., Kasten S., Sinninghe Damsté J. S. and Wagner T. (2015) A continental-weathering control on orbitally driven redox-nutrient cycling during Cretaceous Oceanic Anoxic Event 2. *Geology* **43**, 963–966.

Prescher C., Langenhorst F., Hornemann U. and Deutsch A. (2011) Shock experiments on anhydrite and new constraints on the impact-induced release at the K-Pg boundary. *Meteorit. Planet. Sci.* **46**, 1619–1629.

Raiswell R. and Berner R. A. (1985) Pyrite formation in euxinic and semi-euxinic sediments. *Am. J. Sci.* **285**, 710–724.

Renne P. R., Deino A. L., Hilgen F. J., Kuiper K. F., Mark D. F., Mitchell, III, W. S., Morgan L. E., Mundil R. and Smit J. (2013) Time scales of critical events around the Cretaceous-Paleogene boundary. *Science* **339**, 684–687.

Renne P. R., Sprain C. J., Richards M. A., Self S., Vanderkluysen L. and Pande K. (2015) State shift in Deccan volcanism at the Cretaceous-Paleogene boundary, possibly induced by impact. *Science* **350**, 76–78.

Rennie V. C. F. and Turchyn A. V. (2014) The preservation of $\delta^{34}S_{SO4}$ and $\delta^{18}O_{SO4}$ in carbonate-associated sulfate during marine diagenesis: a 25 Myr test case using marine sediments. *Earth Planet. Sci. Lett.* **395**, 13–23.

Richards M. A., Alvarez W., Self S., Karlstrom L., Renne P. R., Manga M., Sprain C. J., Smit J., Vanderkluysen L. and Gibson S. A. (2015) Triggering of the largest Deccan eruptions by the Chicxulub impact. *Geol. Soc. Am. Bull.* **127**, 1507–1520.

Robinson N., Ravizza G., Coccioni R., Peucker-Ehrenbrink B. and Norris R. D. (2009) A high resolution marine $^{187}Os/^{188}Os$ record for the late Maastrichian: distinguishing the chemical fingerprints of Deccan volcanism and the KP impact event. *Earth Planet. Sci. Lett.* **281**, 159–168.

Robertson D. S., Lewis W. M., Sheehan P. M. and Toon O. B. (2013) K-Pg extinction patterns in marine and freshwater environments: the impact winter model. *J. Geophys. Res.: Biogeosci.* **118**, 1006–1014.

Rooze J., Egger M., Tsandve I. and Slomp C. P. (2016) Iron-dependent anaerobic oxidation of methane in coastal surface sediments: potential controls and impact. *Limnol. Oceanogr.* **00**, 1–26.

Schmidt A., Skeffington R. A., Thordarson T., Self S., Forster P. M., Rap A., Ridgwell A., Fowler D., Wilson M., Mann G. W., Wignall P. B. and Carslaw K. S. (2016) Selective environmental stress from sulfur emitted by continental flood basalt eruptions. *Nat. Geosci.* **9**, 77–82.

Schobben M., Stebbins A., Ghaderi A., Strauss H., Korn D. and Korte C. (2015) Flourishing ocean drives the end-Permian marine mass extinction. *Proc. Natl. Acad. Sci.* **112**, 10298–10303.

Schoene B., Samperton K. M., Eddy M. P., Keller G., Adatte T., Bowring S. A., Khadri S. F. and Gertsch B. (2015) U-Pb geochronology of the Deccan Traps and relation to the end-Cretaceous mass extinction. *Science* **347**, 182–184.

Schoepfer S. D., Tobin T. S., Witts J. D. and Newton R. J. (2017) Intermittent euxinia in the high-latitude James Ross Basin during the latest Cretaceous and earliest Paleocene. *Palaeogeogr. Palaeoclimatol. Palaeoecol.* **477**, 40–54.

Schulte P. D., Alegret L., Arenillas I., Arz J. A., Barton P. J., Bown P. R., Bralower T. J., Chisteson G. L., Claeys P., Cockell C. S., Collins G. S., Deutsch A., Goldin T. J., Goto K., Grajales-Nishimura J. M., Grieve R. A. F., Gulick S. P. S., Johnson K. R., Kiessling W., Koeberl C., Kring D. A., MacLeod K. G., Matsui T., Melosh J., Montanari A., Morgan J. V., Neal C. R., Nichols D. J., Norris R. D., Pierazzo E., Ravizza G., Rebolledo-Vieyra M., Reimold W. U., Robin E., Salge T., Speijer R. P., Sweet A. R., Urrutia-Fucugauchi J., Vajda V., Whalen M. T. and Willumsen P. S. (2010) The Chicxulub asteroid impact and mass extinction at the Cretaceous-Paleogene boundary. *Science* **327**, 1214–1218.

Self S., Schmidt A. and Mather T. A. (2014) Emplacement characteristics, time scales, and volcanic gas release rates of continental flood basalt eruptions on Earth. In: Keller G. and Kerr A. C. (Eds.), Volcanism, Impacts, and Mass Extinctions: Causes and Effects, Geological Society of America Special Paper, vol. 505.

Sepúlveda J., Wendler J., Summons R. E. and Hindrichs K. U. (2009) Rapid resurgence of marine productivity after the Cretaceous-Paleogene mass extinction. *Science* **326**, 129–132.

Sigurdsson H., Bonté P. H., Turpin L., Chaussidon M., Metrich N., Steinberg M., Pradel P. H. and D'Hondt S. (1991) Geochemical constraints on source region of Cretaceous/Tertiary impact glasses. *Nature* **353**, 839–842.

Sigurdsson H., D'Hondt S. and Carey S. (1992) The impact of the Cretaceous/Tertiary bolide on evaporite terrane and the generation of major sulfuric acid aerosol. *Earth Planet. Sci. Lett.* **109**, 543–559.

Sim M. S., Bosak T. and Ono S. (2011) Large sulfur isotope fractionation does not require disproportionation. *Science* **333**, 74–77.

Song H., Tong J., Algeo T. J., Song H., Qiu H., Zhu Y., Tan L., Bates S., Lyons T. W., Luo G. and Kump L. R. (2014) Early Triassic seawater sulfate drawdown. *Geochim. Cosmochim. Ac.* **128**, 95–113.

Staudt W. J. and Schoonen M. A. A. (1995) Sulfate incorporation into sedimentary carbonates. In *Geochemical Transformations of Sedimentary Sulfur* (eds. M. A. Vairavamurthy and M. A. A. Schoonen). American Chemical Society, Washington, pp. 332–345.

Svojtka M., Nyvlt D., Murakami M., Vavrova J., Filip J. and Mixa P. (2009) Provenance and post-depositional low-temperature evolution of the James Ross Basin sedimentary rocks (Antarctic Peninsula) based on fission track analysis. *Antarct. Sci.* **21**, 593–607.

Theiling B. P. and Coleman M. (2015) Refining the extraction methodology of carbonate associated sulfate: Evidence from synthetic and natural carbonate samples. *Chem. Geol.* **411**, 36–48.

Thibault N. (2016) Calcareous nannofossil biostratigraphy and turnover dynamics in the late Campanian-Maastrichtian of the tropical South Atlantic. *Rev. Micropaleontol.* **59**, 57–69.

Timofeeff M. N., Lowenstein T. K., Martins da Silva M. A. and Harris N. B. (2006) Secular variations in the major-ion chemistry of seawater: evidence from fluid inclusions in Cretaceous halites. *Geochim. Cosmochim. Acta* **70**, 1977–1994.

Tobin T. S. and Ward P. D. (2015) Carbon isotope ($\delta^{13}C$) differences between Late Cretaceous ammonites and benthic mollusks from Antarctica. *Palaeogeogr. Palaeoclimatol. Palaeoecol.* **428**, 50–57.

Tobin T. S., Bitz C. M. and Archer D. (2017) Modelling climatic effects of carbon dioxide emissions from the Deccan Traps Volcanic Eruptions around the Cretaceous-Paleogene boundary. *Palaeogeogr., Palaeoclimatol., Palaeoecol.* **478**, 139–148.

Tobin T. S., Ward P. D., Steig E. J., Olivero E. B., Hilburn I. A., Mitchell R. N., Diamond M. R., Raub T. D. and Kirschvink J. L. (2012) Extinction patterns, δ18O trends, and magnetostratigraphy from a southern high-latitude Cretaceous-Paleogene section: links with Deccan volcanism. *Palaeogeogr., Palaeoclimatol. Palaeoecol.* **350–352**, 180–188.

Toon O. B., Bardeen C. and Garcia R. (2016) Designing global climate and atmospheric chemistry simulations for 1 and 10 km diameter asteroid impacts using the properties of ejecta from the K-Pg impact. *Atmos. Chem. Phys.* **16**, 13185–13212.

Turchyn A. V. and Schrag D. P. (2006) Cenozoic evolution of the sulfur cycle: insight from oxygen isotopes in marine sulfate. *Earth Planet. Sci. Lett.* **241**, 763–779.

Turchyn A. V., Antler G., Byrne D., Miller M. and Hodell D. A. (2016) Microbial sulfur metabolism evidenced from pore fluid isotope geochemistry at Site U1385. *Global Planet. Change* **141**, 82–90.

Tyrrell T., Merico A. and McKay D. I. A. (2015) Severity of ocean acidification following the end-Cretaceous asteroid impact. *Proc. Natl. Acad. Sci.* **112**, 6556–6561.

Vellekoop J., Woelders L., Açikalin S., Smit J., van de Schootburgge B., Yilmaz I. Ö., Brinkhuis H. and Speijer R. P. (2017) Ecological response to collapse of the biological pump following the mass extinction at the Cretaceous-Paleogene boundary. *Biogeosciences* **14**, 885–990.

Voigt S., Gale A. S., Jung C. and Jenkyns H. C. (2012) Global correlation of upper Campanian-Maastrichtian successions using carbon-isotope stratigraphy: development of a new Maastrichtian timescale. *Newsl. Stratigr.* **45**, 25–53.

Vonhof H. B. and Smit J. (1997) High-resolution late Maastrichtian–early Danian oceanic $^{87}Sr/^{86}Sr$ record: Implications for Cretaceous-Tertiary boundary events. *Geology* **25**, 347–350.

Wendler I. (2013) A critical evaluation of carbon isotope stratigraphy and biostratigraphic implications for Late Cretaceous global correlation. *Earth Sci. Rev.* **126**, 116–146.

Wilf P., Johnson K. and Huber B. T. (2003) Correlated terrestrial and marine evidence for global climate change before mass extinction at the Cretaceous-Paleogene boundary. *Proc. Nat. Acad. Sci.* **100**, 599–604.

Witts J. D., Whittle R. J., Wignall P. B., Crame J. A., Francis J. E., Newton R. J. and Bowman V. C. (2016) A rapid and severe Cretaceous-Paleogene mass extinction in Antarctica. *Nat. Commun.* **7**, 11738.

Wortmann U. G. and Paytan A. (2012) Rapid variability of seawater chemistry over the past 130 million years. *Science* **337**, 334–336.

Wotte T., Shields-Zhou G. and Strauss H. (2012) Carbonate-associated sulfate: Experimental comparisons of common extraction methods and recommendations toward a standard analytical protocol. *Chem. Geol.* **326–327**, 132–144.

Zachos J. C., Arthur M. A. and Dean W. E. (1989) Geochemical evidence for suppression of pelagic marine productivity at the Cretaceous-Tertiary boundary. *Nature* **337**, 61–64.

Zinsmeister W. J. (1998) Discovery of fish mortality horizon at the K-T boundary on Seymour Island: re-evaluation of events at the end of the Cretaceous. *J. Paleontol.* **72**, 556–571.

Zinsmeister W. J. & Macellari C. E. (1988) Bivalvia (Mollusca) from Seymour Island,). In: Feldmann R. M. and Woodburne M. O. (Eds.), Geology and Paleontology of Seymour Island, Antarctic Peninsula, Geological Society of America, Memoirs, vol. 169, pp. 25–53.

FURTHER READING

Little C. T. S., Birgel D., Boyce A. J., Crame J. A., Francis J. E., Kiel S., Peckmann J., Pirrie D., Rollinson G. K. and Witts J. D. (2015) Late Cretaceous (Maastrichtian) shallow water hydrocarbon seeps from Snow Hill and Seymour Islands, James Ross Basin, Antarctica. *Palaeogeogr. Palaeoclimatol. Palaeoecol.* ***418***, 213–228.

Witts J. D., Bowman V. C., Wignall P. B., Crame J. A., Francis J. E. and Newton R. J. (2015) Evolution and extinction of Maastrichtian (Late Cretaceous) cephalopods from the López de Bertodano Formation, Seymour Island, Antarctica. *Palaeogeogr., Palaeoclimatol. Palaeoecol.* ***418***, 193–212.

Associate Editor: Christian Koeberl